

# A kilonova following a long-duration gamma-ray burst at 350 Mpc

<https://doi.org/10.1038/s41586-022-05390-w>

Received: 22 April 2022

Accepted: 27 September 2022

Published online: 7 December 2022

 Check for updates

Jillian C. Rastinejad<sup>1,2</sup>✉, Benjamin P. Gompertz<sup>3,4</sup>, Andrew J. Levan<sup>5,6</sup>, Wen-fai Fong<sup>1,2</sup>, Matt Nicholl<sup>3,4</sup>, Gavin P. Lamb<sup>7</sup>, Daniele B. Malesani<sup>5,6,8,9</sup>, Anya E. Nugent<sup>1,2</sup>, Samantha R. Oates<sup>3,4</sup>, Nial R. Tanvir<sup>7</sup>, Antonio de Ugarte Postigo<sup>10</sup>, Charles D. Kilpatrick<sup>1,2</sup>, Christopher J. Moore<sup>3,4</sup>, Brian D. Metzger<sup>11,12</sup>, Maria Edvige Ravasio<sup>5,6,13</sup>, Andrea Rossi<sup>14</sup>, Genevieve Schroeder<sup>1,2</sup>, Jacob Jencson<sup>15</sup>, David J. Sand<sup>16</sup>, Nathan Smith<sup>15</sup>, José Feliciano Agüí Fernández<sup>16</sup>, Edo Berger<sup>17</sup>, Peter K. Blanchard<sup>1,2</sup>, Ryan Chornock<sup>18</sup>, Bethany E. Cobb<sup>19</sup>, Massimiliano De Pasquale<sup>20</sup>, Johan P. U. Fynbo<sup>8,9</sup>, Luca Izzo<sup>21</sup>, D. Alexander Kann<sup>16</sup>, Tanmoy Laskar<sup>5,6</sup>, Ester Marini<sup>22</sup>, Kerry Paterson<sup>1,2,23</sup>, Alicia Rouco Escorial<sup>1,2</sup>, Huei M. Sears<sup>1,2</sup> & Christina C. Thöne<sup>24</sup>

Gamma-ray bursts (GRBs) are divided into two populations<sup>1,2</sup>; long GRBs that derive from the core collapse of massive stars (for example, ref.<sup>3</sup>) and short GRBs that form in the merger of two compact objects<sup>4,5</sup>. Although it is common to divide the two populations at a gamma-ray duration of 2 s, classification based on duration does not always map to the progenitor. Notably, GRBs with short ( $\lesssim 2$  s) spikes of prompt gamma-ray emission followed by prolonged, spectrally softer extended emission (EE-SGRBs) have been suggested to arise from compact object mergers<sup>6–8</sup>. Compact object mergers are of great astrophysical importance as the only confirmed site of rapid neutron capture (*r*-process) nucleosynthesis, observed in the form of so-called kilonovae<sup>9–14</sup>. Here we report the discovery of a possible kilonova associated with the nearby (350 Mpc), minute-duration GRB 211211A. The kilonova implies that the progenitor is a compact object merger, suggesting that GRBs with long, complex light curves can be spawned from merger events. The kilonova of GRB 211211A has a similar luminosity, duration and colour to that which accompanied the gravitational wave (GW)-detected binary neutron star (BNS) merger GW170817 (ref.<sup>4</sup>). Further searches for GW signals coincident with long GRBs are a promising route for future multi-messenger astronomy.

On 11 December 2021 at 13:09 UT, the Neil Gehrels Swift Observatory's (Swift) Burst Alert Telescope (BAT) identified the bright GRB 211211A. The burst was discovered simultaneously by the Fermi Gamma-ray Burst Monitor (GBM). The burst's duration of  $51.37 \pm 0.80$  s (ref.<sup>15</sup>) (about 34.3 s in the GBM<sup>16</sup>) and spectral hardness lie close to the mean of the long-GRB population (Fig. 1). The light curve of the burst consists of several overlapping pulses exhibiting little spectral evolution and lasting for approximately 12 s, followed by longer-lived and apparently softer emission extending to 50 s. Although GRB 211211A's lack of early spectral evolution and later softening is reminiscent of the behaviour of past EE-SGRBs, these durations are far beyond those considered in previous searches for EE-SGRBs<sup>7,17</sup>. The Swift X-ray Telescope (XRT) and

Ultra-Violet Optical Telescope (UVOT) began observing the accompanying broadband afterglow about 1 min after the burst (see Methods section 'Swift observations').

Motivated by the gamma-ray light curve of GRB 211211A and its proximity to the bright ( $r = 19.4$  mag) galaxy Sloan Digital Sky Survey (SDSS) J140910.47+275320.8 (Fig. 2), we initiated multi-wavelength follow-up observations. We obtained spectroscopy at the Nordic Optical Telescope (NOT; later confirmed with a Keck II spectrum; see Methods section 'Host galaxy observations'), which showed that the nearby galaxy is at a redshift  $z = 0.0763 \pm 0.0002$  (distance  $\approx 350$  Mpc). The modest offset between the galaxy and optical afterglow ( $5.44^\circ \pm 0.02^\circ$ ;  $7.91 \pm 0.03$  kpc in projection), their low probability of chance coincidence

<sup>1</sup>Center for Interdisciplinary Exploration and Research in Astrophysics, Northwestern University, Evanston, IL, USA. <sup>2</sup>Department of Physics and Astronomy, Northwestern University, Evanston, IL, USA. <sup>3</sup>Institute for Gravitational Wave Astronomy, University of Birmingham, Birmingham, UK. <sup>4</sup>School of Physics and Astronomy, University of Birmingham, Birmingham, UK. <sup>5</sup>Department of Astrophysics, Radboud University, Nijmegen, The Netherlands. <sup>6</sup>Institute for Mathematics, Astrophysics and Particle Physics (IMAPP), Radboud University, Nijmegen, The Netherlands. <sup>7</sup>School of Physics and Astronomy, University of Leicester, Leicester, UK. <sup>8</sup>Cosmic Dawn Center (DAWN), Copenhagen, Denmark. <sup>9</sup>Niels Bohr Institute, University of Copenhagen, Copenhagen, Denmark. <sup>10</sup>Artemis, Université Côte d'Azur, Observatoire de la Côte d'Azur, CNRS, Nice, France. <sup>11</sup>Center for Computational Astrophysics, Flatiron Institute, New York, NY, USA. <sup>12</sup>Department of Physics, Columbia Astrophysics Laboratory, Columbia University, New York, NY, USA. <sup>13</sup>INAF, Astronomical Observatory of Brera, Merate, Italy. <sup>14</sup>INAF, Osservatorio di Astrofisica e Scienza dello Spazio, Bologna, Italy. <sup>15</sup>Steward Observatory, University of Arizona, Tucson, AZ, USA. <sup>16</sup>Instituto de Astrofísica de Andalucía (IAA-CSIC), Granada, Spain. <sup>17</sup>Center for Astrophysics, Harvard & Smithsonian, Cambridge, MA, USA. <sup>18</sup>Department of Astronomy, University of California, Berkeley, Berkeley, CA, USA. <sup>19</sup>Department of Physics, The George Washington University, Washington, DC, USA. <sup>20</sup>Department of Mathematical and Computer Science, Physical Sciences and Earth Sciences, Polo Papardo, University of Messina, Messina, Italy. <sup>21</sup>Dark Cosmology Centre, University of Copenhagen, Copenhagen, Denmark. <sup>22</sup>INAF, Observatory of Rome, Monte Porzio Catone, Italy. <sup>23</sup>Max-Planck-Institut für Astronomie (MPIA), Heidelberg, Germany. <sup>24</sup>Astronomical Institute of the Czech Academy of Sciences (ASU-CAS), Ondřejov, Czech Republic. ✉e-mail: jillianrastinejad2024@u.northwestern.edu

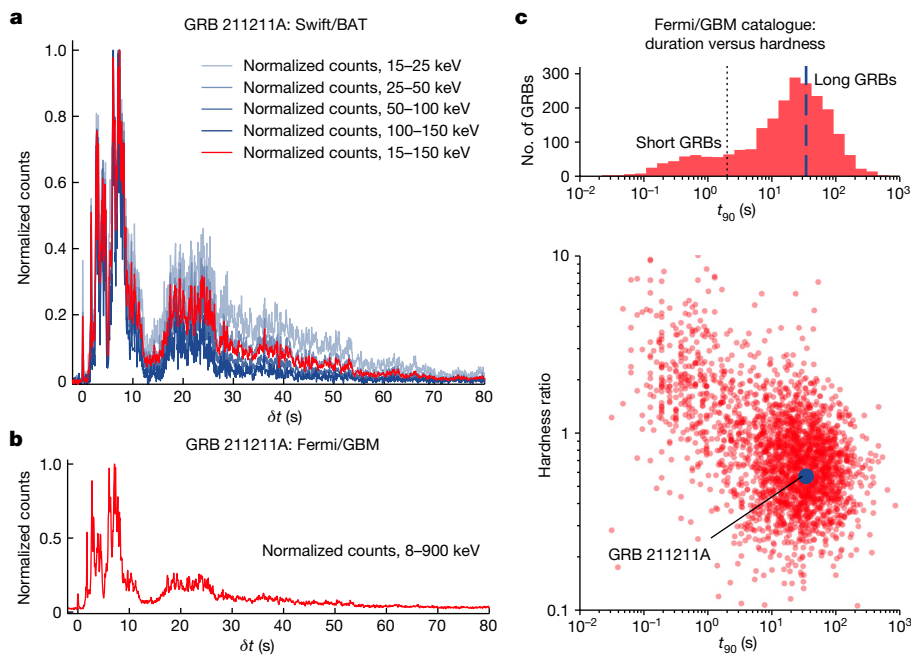


**Fig. 1 | Swift/BAT and Fermi/GBM gamma-ray light curves of GRB 211211A.**

**a–c**, The light curves show similarities with both long GRBs and EE-SGRBs. We separate the Swift/BAT light curve by band (**a**; blue) and normalized by the maximum number of counts in each band. The red curve is the light curve across all four bands and is also normalized by the maximum counts. The two initial spikes (lasting about 4 s and about 8 s) are prominent in each of the bands shown, whereas the tail ( $\geq 12$  s) becomes softer over time. Although this soft tail

is similar to the behaviour of past EE-SGRBs (for example, GRB 060614 (ref. <sup>8</sup>)), its initial pulses are longer than those previously observed in EE-SGRBs. The Fermi/GBM light curve of GRB 211211A shows a similar structure to that of BAT (**b**). We also show the hardness ratio (**c**; the ratio of 50–300-keV to 10–50-keV photon fluxes) versus  $t_{90}$  for GRBs in the Fermi/GBM GRB catalogue<sup>40</sup>. The  $t_{90}$  time-averaged properties of GRB 211211A (blue) are typical of long GRBs, which occupy the lower-right corner of the parameter space.

(1.4% (ref. <sup>18</sup>)) and the absence of any fainter, underlying host galaxy in late-time Hubble Space Telescope (HST) imaging provide compelling evidence that GRB 211211A originated in SDSS J140910.47+275320.8 (Fig. 2). At 350 Mpc, GRB 211211A is one of the closest bursts across both short and long classes discovered so far.

We obtained optical imaging with the NOT and the Calar Alto Observatory (CAHA) that showed an uncatalogued source fading rapidly over the first 3 days post-burst. At 4.1 days, we observed in the  $K$ -band with Gemini North, detecting a  $K = 22.4$  mag source, indicative of a

strong infrared excess compared with the optical afterglow light curve. We continued to observe in the  $iJK$ -bands with Gemini North and the MMT to 10 days post-burst. At 6.3 days, we obtained a deep limit on the 6-GHz radio afterglow with the Karl G. Jansky Very Large Array (VLA). We acquired late-time optical and near-infrared (NIR) observations with Gemini North, MMT, the Large Binocular Telescope (LBT), Gran Telescopio Canarias (GTC) and HST. We obtained NOT imaging at 17.7 days post-burst that constrains an associated supernova (SN) to deep limits ( $vL_v < 3 \times 10^{40}$  erg s $^{-1}$ , or  $M_i > -13$  mag). This rules out a typical

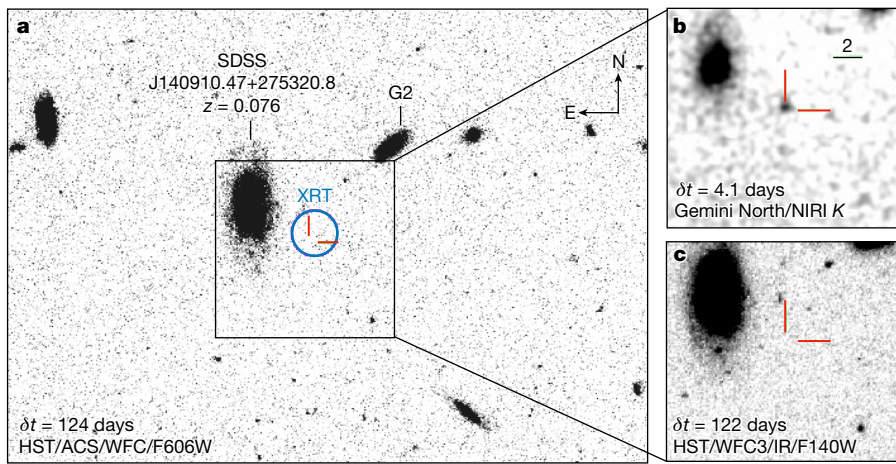


**Fig. 2 | The field of GRB 211211A in HST and Gemini North imaging.**

**a–c**, Late-time HST F606W and F140W images (**a** and **c**, respectively) covering the position of the Swift/XRT afterglow (blue circle) and the NIR counterpart (red crosshairs). We label the putative host, SDSS J140910.47+275320.8 ( $z = 0.076$ ), which is offset 5.44'' from the NIR counterpart and a second nearby

galaxy, G2 (see Methods section ‘Strong evidence in favour of  $z = 0.076$  origin’). No source is detected at the position of the NIR counterpart to a depth of F606W  $> 27.8$  mag. A smoothed Gemini North/NIRI  $K$ -band image at 4.1 days post-burst detects a  $K = 22.4$  mag point source at the position of the optical afterglow of GRB 211211A (**b**). Scale bar in panel **b**, 2'' or about 3 kpc.

long GRB massive star origin to limits a factor of >200 fainter than the prototype GRB-SN1998bw (assuming  $z = 0.076$  (ref. <sup>3</sup>)). We present the full optical-NIR dataset for the counterpart of GRB 211211A in Extended Data Table 1 and describe the data reduction and analysis further in Methods (see sections ‘Optical afterglow observations’ and ‘Further optical-NIR observations’). Notably, in the  $K$ -band, the luminosity at 4.1 days post-burst is approximately that of astronomical transient (AT) 2017gfo ( $vL_v \approx 8 \times 10^{40} \text{ erg s}^{-1}$ ) and the light curve fades at a remarkably similar rate to AT 2017gfo (Fig. 3).

We first fit an afterglow model following the methods of ref. <sup>19</sup> (and references therein; see Methods section ‘Afterglow model’) to the full X-ray and radio light curves, and to the ultraviolet (UV)-optical-NIR photometry at  $\delta t < 0.1$  days (in which  $\delta t$  denotes the time after the BAT trigger), when the afterglow is expected to dominate any thermal counterpart. We find an isotropic-equivalent kinetic energy,  $E_{K,\text{iso}} = 5 \times 10^{52} \text{ erg}$ . Other properties are listed in Extended Data Table 3, and are consistent with those inferred for previous short GRBs. The  $K$ -band observation at 4.1 days is in excess of about 3.8 mag (a factor of 33 in brightness) compared with the corresponding model afterglow flux, which is well constrained by the X-ray and radio data, necessitating an extra component in our model.

We thus obtain optical-NIR photometry after the subtraction of the afterglow component and considering the uncertainty in the afterglow model (Extended Data Table 1). We fit the afterglow-subtracted photometry with a three-component kilonova model following refs. <sup>20,21</sup> (see Methods section ‘Kilonova model’). Our fitting indicates a total  $r$ -process ejecta mass of  $M_{\text{ej}} = 0.047^{+0.026}_{-0.011} M_\odot$ . This includes about  $0.02 M_\odot$  of lanthanide-rich (‘red’) ejecta with velocity  $v \approx 0.3c$ , in which  $c$  is the speed of light, and about  $0.01 M_\odot$  of intermediate-opacity (‘purple’) ejecta with  $v \approx 0.1c$ . Red ejecta can be produced in dynamical tides<sup>22</sup> or by winds from a remnant accretion disk if neutrino irradiation is low<sup>23</sup>, although the high velocity found by our model is more consistent with a tidal origin. The purple ejecta are consistent with a disk wind, assuming moderate neutrino irradiation to lower the lanthanide fraction. The remaining roughly  $0.01 M_\odot$  is lanthanide-free (‘blue’) material with  $v \approx 0.3c$ . This can be produced by dynamical shocks<sup>24</sup>, winds from a long-lived magnetized neutron star (NS) (magnetar) remnant<sup>25</sup> or from a disk wind with high neutrino irradiation. The blue ejecta mainly produce optical emission on timescales of about 1 day and, hence, are slightly degenerate with early shock cooling of matter heated by the GRB jet<sup>26</sup> (see Methods section ‘Kilonova model’). Overall, our best-fit masses are in reasonable agreement with estimates for AT 2017gfo, although the reddest ejecta seem to be more massive in this case (Extended Data Fig. 8). If we assume that the progenitor binary consists of two NSs and use predictions from merger simulations to constrain the relative component masses and velocities<sup>21</sup>, we obtain a good fit with a  $1.4 + 1.3 M_\odot$  binary producing about  $0.02 M_\odot$  of ejecta, although matching the luminosity in the first day may require further heating by the GRB jet over the minute-long timescale of the burst (see Methods section ‘Kilonova model’; Extended Data Figs. 4 and 5).

Although the profile of the initial gamma-ray pulse complex has a duration  $\gg 2$  s, there are further lines of evidence (beyond the kilonova) that link GRB 211211A to a compact object merger. First, the observed exponential decline in X-rays at a few hundred seconds after trigger is a notable feature of EE-SGRBs<sup>27</sup> and is highly consistent with both the luminosity and the timescale of previous examples. Second, the spectral lag during the initial burst of  $4 \pm 9$  ms between the 25–50-keV and 100–150-keV BAT bands is more consistent with short than long GRBs (see Methods section ‘Alternative interpretations’<sup>28</sup>). The host galaxy stellar population has mass approximately equal to  $7 \times 10^8 M_\odot$  and star formation rate (SFR) of about  $0.07 M_\odot \text{ year}^{-1}$  (specific SFR of around  $0.10 \text{ Gyr}^{-1}$ ), which are more consistent with the hosts of short than long GRBs (see Methods section ‘Stellar population modelling of SDSSJ140910.47+275320.8’)<sup>29,30</sup>. The host offset and the lack of any

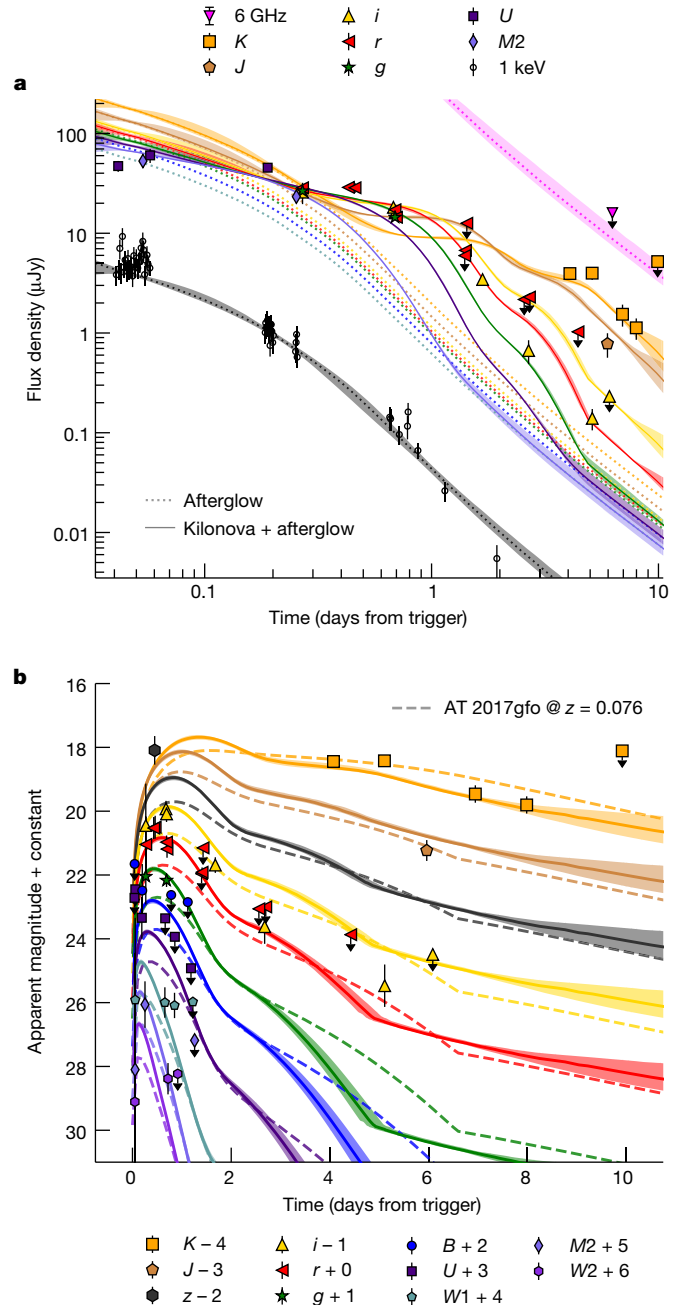


**Fig. 3 | Afterglow and kilonova models fit to selected observations of the broadband counterpart of GRB 211211A.** Modelling strongly supports the detection of an  $r$ -process-enriched component. **a**, Relevant detections and their  $1\sigma$  uncertainties and  $3\sigma$  upper limits, alongside the superimposed kilonova and afterglow models (solid lines) and the afterglow model alone (dotted lines). The afterglow model is well constrained by the radio and X-ray light curves and provides a good fit to the optical data at  $\leq 0.1$  day post-burst. The NIR detections are approximately four magnitudes brighter than that predicted by the afterglow model and require a kilonova component to fit. **b**, The kilonova model (solid lines) provides a reasonable fit to the afterglow-subtracted optical-NIR light curve. We also plot models tuned to AT 2017gfo from ref. <sup>21</sup> shifted to the redshift of GRB 211211A (dashed lines). The  $K$ -band light curves are approximately the same luminosity at 4.1 days post-burst and fade on similar timescales.

underlying stellar component can be readily explained in merger scenarios, but would be extremely unusual for a massive star.

It is also relevant to consider whether the counterpart could instead arise from a core-collapse or Ni-powered event, either at  $z = 0.076$  or

from a more distant, and as yet unseen, galaxy. Notably, our NOT limit of  $i > 24.7$  mag rules out any known GRB-SN at  $z = 0.076$  and would have been sensitive to GRB-supernovae (SNe) out to  $z \approx 0.5$  (see Methods section ‘Alternative interpretations’). The K-band peak and temporal evolution of GRB 211211A are not compatible with any SN in the sample of ref.<sup>31</sup>, including SN 2010bh<sup>32</sup>, the dimmest, fastest-fading GRB-SN considered. There is also no sign of substantial stellar mass or star formation at the burst location that might obscure the SN with dust (Fig. 2), nor is there evidence of marked absorption in the host spectral energy distribution, which extends to  $<2,000$  Å. Furthermore, light-curve models powered by  $^{56}\text{Ni}$  decay (relevant for an SN or possibly a merger between a NS and a white dwarf<sup>33</sup>) are unable to provide satisfactory fits to our data (Methods section ‘ $^{56}\text{Ni}$ -powered transient model’; Extended Data Fig. 6). Higher-redshift scenarios are limited by several observational constraints. First, the detection in the Swift *uw2* band demonstrates no absorption from neutral hydrogen at 1,928 Å (observed), implying  $z < 1.4$  (99% confidence level). Furthermore, deep HST observations reach  $F606\text{W} > 27.8$  mag and  $F140\text{W} > 27.2$  mag ( $3\sigma$  confidence). At these depths, we would have detected all known long and short GRB host galaxies at  $z < 1.4$  (refs.<sup>34,35</sup>). An underlying, unseen dwarf galaxy of G2 (Fig. 2) hosting a dust-obscured SN is also difficult to reconcile, as low-mass galaxies have, in general, lower dust contents (see Methods section ‘Alternative interpretations’). We conclude that a kilonova is the most natural explanation of the known channels to reproduce our observations of GRB 211211A.

The interpretation of the NIR excess as an *r*-process kilonova in turn implies that GRB 211211A originated in a compact object merger. We briefly explore several explanations for extended gamma-ray emission following such an event. First, the extended emission may be explained by a relativistic wind imparted by a magnetar remnant (for example, ref.<sup>36</sup>). The progenitor may also have been a NS–black hole (BH) system. Tidal disruption of the NS would cause further mass to fall back onto the remnant for several seconds following the merger and be launched in the jet, producing extended emission (for example, refs.<sup>37,38</sup>). However, we note that the moderate-sized blue component of the kilonova is not consistent with such a scenario. A BNS merger with a strongly asymmetric mass ratio provides a similar but alternative explanation, but may also struggle to produce sufficient blue ejecta. Future detections of GRBs and kilonovae in tandem with inferred properties from GW observations, which provide insight to the total and component masses of the progenitor system, will disclose the source of gamma-ray extended emission. The detection of a kilonova following a long GRB implies that the current NS merger rates calculated from short GRBs (for example, ref.<sup>39</sup>) may underestimate the true population.

GRB 211211A lies at a luminosity distance of 350 Mpc. This distance is only slightly beyond the sky and orientation-averaged horizon for the LIGO/Virgo detectors at design sensitivity. Notably, sensitivity is maximized for face-on mergers (that is, events with GRBs pointed in our direction). Using GW template waveforms and expected noise curves (see Methods section ‘GW detection significance’), we calculate the expected signal-to-noise ratio (S/N) for a  $1.4 + 1.4 M_{\odot}$  binary merger at 350 Mpc during the third (O3), fourth (O4) and fifth (O5) observing runs, finding S/Ns of 7.4, 11.9 and 18.9, respectively. The S/N is even higher in the case of a fiducial  $1.4 + 5 M_{\odot}$  NS–BH merger (and S/N > 10 in O3), demonstrating that a GRB 211211A-like event would be detectable in upcoming observing runs. Indeed, because the time coincidence of GW and GRB emission and the known sky location can be used to increase the sensitivity of the GW detectors, such long GRB/GW coincidences can increase the number of multi-messenger signals that can be recovered in the future.

## Online content

Any methods, additional references, Nature Portfolio reporting summaries, source data, extended data, supplementary information,

acknowledgements, peer review information; details of author contributions and competing interests; and statements of data and code availability are available at <https://doi.org/10.1038/s41586-022-05390-w>.

- Norris, J. P., Cline, T. L., Desai, U. D. & Teegarden, B. J. Frequency of fast, narrow γ-ray bursts. *Nature* **308**, 434–435 (1984).
- Kouveliotou, C. et al. Identification of two classes of gamma-ray bursts. *Astrophys. J.* **413**, L101–L104 (1993).
- Galama, T. J. et al. An unusual supernova in the error box of the γ-ray burst of 25 April 1998. *Nature* **395**, 670–672 (1998).
- Abbott, B. P. et al. Multi-messenger observations of a binary neutron star merger. *Astrophys. J.* **848**, L12 (2017).
- Goldstein, A. et al. An ordinary short gamma-ray burst with extraordinary implications: *Fermi*-GBM detection of GRB 170817A. *Astrophys. J.* **848**, L14 (2017).
- Norris, J. P. Implications of the lag-luminosity relationship for unified gamma-ray burst paradigms. *Astrophys. J.* **579**, 386–403 (2002).
- Norris, J. P. & Bonnell, J. T. Short gamma-ray bursts with extended emission. *Astrophys. J.* **643**, 266–275 (2006).
- Gehrels, N. et al. A new γ-ray burst classification scheme from GRB 060614. *Nature* **444**, 1044–1046 (2006).
- Arcavi, I. et al. Optical emission from a kilonova following a gravitational-wave-detected neutron-star merger. *Nature* **551**, 64–66 (2017).
- Coulter, D. A. et al. Swope Supernova Survey 2017a (SSS17a), the optical counterpart to a gravitational wave source. *Science* **358**, 1556–1558 (2017).
- Lipunov, V. M. et al. MASTER optical detection of the first LIGO/Virgo neutron star binary merger GW170817. *Astrophys. J.* **850**, 1 (2017).
- Tanvir, N. R. et al. The emergence of a lanthanide-rich kilonova following the merger of two neutron stars. *Astrophys. J.* **848**, L27 (2017).
- Soares-Santos, M. The Dark Energy Survey and The Dark Energy Camera GW-EM Collaboration et al. The electromagnetic counterpart of the binary neutron star merger LIGO/Virgo GW170817. I. Discovery of the optical counterpart using the dark energy camera. *Astrophys. J.* **848**, L16 (2017).
- Valenti, S. et al. The discovery of the electromagnetic counterpart of GW170817: kilonova AT 2017gfo/DLT17ck. *Astrophys. J.* **848**, L24 (2017).
- Stamatikos, M. et al. GRB 211211A: Swift-BAT refined analysis. GRB Coordinates Network, Circular Service, No. 31209 (2021).
- Mangan, J., Dunwoody, R. & Meegan, C.; Fermi GBM Team. GRB 211211A: Fermi GBM observation. GRB Coordinates Network, Circular Service, No. 31210 (2021).
- Kaneko, Y., Bostancı, Z. F., Göğüş, E. & Lin, L. Short gamma-ray bursts with extended emission observed with *Swift*/BAT and *Fermi*/GBM. *Mon. Not. R. Astron. Soc.* **452**, 824–837 (2015).
- Bloom, J. S., Kulkarni, S. R. & Djorgovski, S. G. The observed offset distribution of gamma-ray bursts from their host galaxies: a robust clue to the nature of the progenitors. *Astron. J.* **123**, 1111–1148 (2002).
- Lamb, G. P. et al. GRB jet structure and the jet break. *Mon. Not. R. Astron. Soc.* **506**, 4163–4174 (2021).
- Villar, V. A. et al. The combined ultraviolet, optical, and near-infrared light curves of the kilonova associated with the binary neutron star merger GW170817: unified data set, analytic models, and physical implications. *Astrophys. J. Lett.* **851**, L21 (2017).
- Nicholl, M. et al. Tight multimessenger constraints on the neutron star equation of state from GW170817 and a forward model for kilonova light-curve synthesis. *Mon. Not. R. Astron. Soc.* **505**, 3016–3032 (2021).
- Sekiguchi, Y., Kiuchi, K., Kyutoku, K. & Shibata, M. Dynamical mass ejection from binary neutron star mergers: radiation-hydrodynamics study in general relativity. *Phys. Rev. D* **91**, 064059 (2015).
- Metzger, B. D. & Fernández, R. Red or blue? A potential kilonova imprint of the delay until black hole formation following a neutron star merger. *Mon. Not. R. Astron. Soc.* **441**, 3444–3453 (2014).
- Bauswein, A., Goriely, S. & Janka, H.-T. Systematics of dynamical mass ejection, nucleosynthesis, and radioactively powered electromagnetic signals from neutron-star mergers. *Astrophys. J.* **773**, 78 (2013).
- Metzger, B. D., Thompson, T. A. & Quataert, E. A magnetar origin for the kilonova ejecta in GW170817. *Astrophys. J.* **856**, 101 (2018).
- Piro, A. L. & Kollmeier, J. A. Evidence for cocoon emission from the early light curve of SSS17a. *Astrophys. J.* **855**, 103 (2018).
- Gompertz, B. P., O’Brien, P. T., Wynn, G. A. & Rowlinson, A. Can magnetar spin-down power extended emission in some short GRBs? *Mon. Not. R. Astron. Soc.* **431**, 1745–1751 (2013).
- Bernardini, M. G. et al. Comparing the spectral lag of short and long gamma-ray bursts and its relation with the luminosity. *Mon. Not. R. Astron. Soc.* **446**, 1129–1138 (2015).
- Nugent, A. E. et al. Short GRB host galaxies II: a legacy sample of redshifts, stellar population properties, and implications for their neutron star merger origins. Preprint at <https://arxiv.org/abs/2206.01764> (2022).
- Perley, D. A. et al. A population of massive, luminous galaxies hosting heavily dust-obscured gamma-ray bursts: implications for the use of GRBs as tracers of cosmic star formation. *Astrophys. J.* **778**, 128 (2013).
- Cano, Z. Gamma-ray burst supernovae as standardizable candles. *Astrophys. J.* **794**, 121 (2014).
- Olivares, E. F. et al. The fast evolution of SN 2010bh associated with XRF 100316D. *Astron. Astrophys.* **539**, A76 (2012).
- King, A., Olsson, E. & Davies, M. B. A new type of long gamma-ray burst. *Mon. Not. R. Astron. Soc.* **374**, 34–36 (2007).

34. Leibler, C. N. & Berger, E. The stellar ages and masses of short gamma-ray burst host galaxies: investigating the progenitor delay time distribution and the role of mass and star formation in the short gamma-ray burst rate. *Astrophys. J.* **725**, 1202–1214 (2010).
35. Lyman, J. D. et al. The host galaxies and explosion sites of long-duration gamma ray bursts: *Hubble Space Telescope* near-infrared imaging. *Mon. Not. R. Astron. Soc.* **467**, 1795–1817 (2017).
36. Metzger, B. D., Quataert, E. & Thompson, T. A. Short-duration gamma-ray bursts with extended emission from protomagnetar spin-down. *Mon. Not. R. Astron. Soc.* **385**, 1455–1460 (2008).
37. Metzger, B. D., Arcones, A., Quataert, E. & Martínez-Pinedo, G. The effects of *r*-process heating on fallback accretion in compact object mergers. *Mon. Not. R. Astron. Soc.* **402**, 2771–2777 (2010).
38. Desai, D., Metzger, B. D. & Foucart, F. Imprints of *r*-process heating on fall-back accretion: distinguishing black hole-neutron star from double neutron star mergers. *Mon. Not. R. Astron. Soc.* **485**, 4404–4412 (2019).
39. Fong, W., Berger, E., Margutti, R. & Zauderer, B. A. A decade of short-duration gamma-ray burst broadband afterglows: energetics, circumburst densities, and jet opening angles. *Astrophys. J.* **815**, 102 (2015).
40. von Kienlin, A. et al. The fourth Fermi-GBM gamma-ray burst catalog: a decade of data. *Astrophys. J.* **893**, 46 (2020).

**Publisher's note** Springer Nature remains neutral with regard to jurisdictional claims in published maps and institutional affiliations.

Springer Nature or its licensor (e.g. a society or other partner) holds exclusive rights to this article under a publishing agreement with the author(s) or other rightsholder(s); author self-archiving of the accepted manuscript version of this article is solely governed by the terms of such publishing agreement and applicable law.

© The Author(s), under exclusive licence to Springer Nature Limited 2022

# Article

## Methods

Unless otherwise stated, we report all observations in AB mag units and all times in the observer's frame. We use a standard cosmology of  $H_0 = 69.6 \text{ km s}^{-1} \text{ Mpc}^{-1}$ ,  $\Omega_M = 0.286$  and  $\Omega_{\text{vac}} = 0.714$  throughout this work<sup>41</sup>.

### GRB detection

The refined Swift/BAT position localizes GRB 211211A to right ascension (RA) = 14h 09 m 05.2 s, declination (dec.) = +27° 53' 03.8" with an uncertainty of 1' (ref. <sup>15</sup>). GRB 211211A was also identified by the GBM on board the Fermi Gamma-ray Space Telescope with a consistent localization<sup>16,42</sup>. The burst was further detected by the CALET Gamma-ray Burst Monitor<sup>43,44</sup> and the INTEGRAL SPI-ACS<sup>45,46</sup>.

### Swift observations

The Swift XRT<sup>47</sup> observed the field of GRB 211211A from  $\delta t = 69$  s to 74.2 ks (in which  $\delta t$  is time since the BAT trigger), identifying an uncatalogued X-ray source at a refined position of RA = 14 h 09 m 10.08 s, dec. = +27° 53' 18.8" with an uncertainty of 1.9".

X-ray data are downloaded from the UK Swift Science Data Centre (UKSSDC)<sup>48,49</sup>. We take the 0.3–10-keV flux light curve and convert it to 1-keV flux density (compared with ref. <sup>50</sup>) using the photon index of 1.51 from the late-time-averaged photon-counting spectrum on the UKSSDC<sup>48,49</sup>. The early X-ray light curve (taken in windowed timing mode) shows a bright plateau with a 0.3–10-keV flux of about  $3 \times 10^{-8} \text{ erg s}^{-1} \text{ cm}^{-2}$ . Its subsequent rapid decay at a rate of  $\gg t^{-3}$  indicates an internal origin for the emission. Photon-counting-mode data taken from several thousand seconds after trigger show a shallower power-law evolution, consistent with the emergence of the afterglow.

The Swift/UVOT began settled observations of the field of GRB 211211A 88 s after the BAT trigger. The afterglow was detected in all of the UVOT filters. To reduce contamination from the nearby galaxy, source counts were extracted from the UVOT image mode data using a source region of 3" radius. To be consistent with the UVOT calibration, these count rates were then corrected to 5" using the curve of growth contained in the calibration files. Background counts were extracted using a circular region of radius 20" located in a source-free region near to the GRB. The count rates were obtained from the image lists using the Swift tool uvotsource. They were converted to magnitudes using the UVOT photometric zero points<sup>51,52</sup>. To improve the S/N, the count rates in each filter were binned using  $\Delta t = 0.2\delta t$ . We report all UVOT photometry in Extended Data Table 2. The detection of the afterglow in six Swift/UVOT filters strongly supports a  $z \lesssim 1.4$  origin for GRB 211211A (99% confidence level).

### Radio observation

We initiated 6-GHz (C-band) VLA observations of GRB 211211A at  $\delta t = 6.27$  days (programme no. 21B-198; Principal Investigator: Fong). We used 3C286 for flux and band-pass calibration and J1407+2827 for gain calibration. We used the Common Astronomy Software Applications (CASA) pipeline products for data calibration and analysis<sup>53</sup>, and imaged the source using CASA/tclean, using a Briggs weighting and robustness parameter of 0.5. No source is detected at the position of the X-ray afterglow to a  $3\sigma$  ( $5\sigma$ ) upper limit of 9.6  $\mu\text{Jy}$  (16  $\mu\text{Jy}$ ). We use the more conservative  $5\sigma$  upper limit in our analysis to account for any effects from scintillation.

### Optical afterglow observations

At 16.6 h post-burst, we obtained *gri*-band imaging and spectroscopy of the GRB counterpart and putative host galaxy<sup>54</sup>, using the Alhambra Faint Object Spectrograph and Camera (ALFOSC) mounted on the 2.6-m NOT. We reduce the images using standard techniques and find that the afterglow is well detected in all filters. We flux calibrate images using standard stars in the field from the Pan-STARRS catalogue<sup>55</sup>. We obtained spectroscopy using grism #4, which covers the wavelength

range 3,500–9,500 Å at resolution  $\lambda/\Delta\lambda = 350$ . We oriented the slit to cover both the counterpart and the nearby galaxy. We detect a featureless continuum from the transient, hampering a direct redshift measurement (Extended Data Fig. 1).

We obtained four epochs of *i*-band imaging with the Calar Alto Faint Object Spectrograph mounted on the 2.2-m CAHA telescope over  $\delta t = 0.7$ –19.6 days (programme no. 21B-2.2-018; Principal Investigator: de Ugarte Postigo). We reduce images following standard procedures in IRAF. We perform aperture photometry on the images with IRAF/phot (ref. <sup>56</sup>).

### Further optical-NIR observations

We initiated NIR observations with the Near-Infrared Imager (NIRI)<sup>57</sup> mounted on the 8-m Gemini North telescope (programme no. GN2021B-Q-109; Principal Investigator: Fong) on 15 December 2021 ( $\delta t = 4.1$  days). We detect a *K*-band source at RA = 14 h 09 m 10.119 s, dec. = +27° 53' 18.03" (error of 0.19"), consistent with the X-ray and optical afterglow positions. We continued to observe approximately nightly in the *i*-band, *J*-band and/or *K*-band with NIRI and the Gemini Multiple Object Spectrographs (GMOS)<sup>58</sup> on Gemini North and the MMT and Magellan Infrared Spectrograph (MMIRS) mounted on the 6.5-m MMT<sup>59</sup> (programme nos. UAO-G178-21B and UAO-S127-21B; Principal Investigators: Rastinejad, Smith) until 21 December 2021 ( $\delta t = 9.98$  days).

We reduced NIRI images using the Gemini DRAGONS pipeline<sup>60</sup>, and GMOS and MMIRS images with a custom Python pipeline, POTPyRI<sup>61</sup>. Images were astrometrically registered to SDSS or the Gaia catalogue using standard IRAF tasks, the Gaia software or astrometry.net<sup>62</sup>. Between  $\delta t = 4.1$  and 8.0 days, our NIR observations clearly detect a source at the position of the optical afterglow. To ensure that no host galaxy flux is contaminating our photometric values, we obtained a deep *i*-band template image of the field at  $\delta t \approx 55$  days with Gemini North/GMOS. Further, we obtained deep *K*-band and *K<sub>s</sub>*-band template images of the field at  $\delta t \approx 66$ , 88 and 98 days with the Espectrógrafo Multiobjeto InfraRojo (EMIR) mounted on the 10.4-m GTC (programme no. GTCMULTIPLE2H-21B; Principal Investigator: de Ugarte Postigo), MMT/MMIRS and the LBT Near Infrared Spectroscopic Utility with Camera and Integral Field Unit for Extragalactic Research (LUCI)<sup>63</sup> mounted on the dual 8.4-m mirrored LBT (programme no. IT-2021B-018; Principal Investigator: Palazzi), respectively. We reduce the EMIR data using a self-designed pipeline based on shell scripts and IRAF tasks and the LBT *K<sub>s</sub>*-band image using the data-reduction pipeline developed at Osservatorio Astronomico di Roma (INAF<sup>64</sup>).

We aligned the images using standard IRAF tasks and perform image subtractions using HOTPANTS<sup>65</sup>. For the *i*-band image at  $\delta t = 5.1$  days, we clearly detect a residual in the subtraction. Owing to the faintness of the NIR detections and the added noise of image subtraction, no source is detected in the *K*-band residuals. However, our template image allows us to place limits on any underlying source contribution to  $K_s > 24.6$  mag ( $3\sigma$ ).

We calibrate the Gemini North/GMOS, MMT/MMIRS, GTC/EMIR and LBT/LUCI images using stars in common with SDSS Data Release 12 (DR12 (ref. <sup>66</sup>)) and Two Micron All-Sky Survey (2MASS<sup>67</sup>). Owing to the narrow field of view of the NIRI and the resulting dearth of 2MASS standard stars, we calibrate NIRI images using stars in common with the MMIRS image taken at  $\delta t = 7.98$  days, whose magnitudes we have measured from comparison with 2MASS. We perform aperture photometry at the position of the afterglow using the IRAF/phot task on the *i*-band subtracted image and the *J*-band and *K*-band images directly. We derive upper limits on the Gemini, LBT and MMT images by measuring the magnitudes of  $3\sigma$  sources in the field using an aperture approximately proportional to the full width at half maximum of the transient.

Finally, at 17.6 days post-burst, we obtained *i*-band imaging of the field with the NOT/ALFOSC. We do not detect a source at the position of the optical-NIR counterpart to a  $3\sigma$  limiting magnitude of  $i > 24.7$  AB mag. We report all photometry in Extended Data Table 1

and plot spectral energy distributions (SEDs) of the UV-optical-NIR counterpart to GRB 211211A at five approximately contemporaneous epochs in Extended Data Fig. 2.

## HST observations

On 12 and 14 April 2022, we observed the field of GRB 211211A using the HST with WFC3/IR/F140W and ACS/WFC/F606W, respectively (programme no. 16923; Principal Investigator: Rastinejad). We reduced the images using the custom pipeline `hst123` (ref. <sup>68</sup>), which uses the astrodrizzle package to reduce and align the images (see ref. <sup>69</sup> for details). We performed aperture photometry on SDSS J140910.47+275320.8 using a 5'' aperture in the drizzled images and using zero points calculated for the drizzled frames by `hst123`. After aligning our HST data to our *K*-band Gemini image from  $\delta t = 4.1$  days, we place upper limits on the presence of an HST counterpart using artificial star injection at the NIR counterpart position. Using the fake star methods in `dolphot`<sup>70</sup>, we inject 50,000 artificial stars in increments of 0.01 mag. We then estimate the magnitude threshold at which 99.7% of sources are recovered at  $3\sigma$ , which we consider to be the  $3\sigma$  limiting magnitude. No source is detected at the position of the optical afterglow to  $F_{606W} > 27.76$  mag and  $F_{140W} > 27.19$  AB mag. We list further multi-band limits for an underlying source from ground-based telescopes in Extended Data Table 1.

Our HST upper limits eliminate the presence of an underlying host with the brightness of any known short and long GRB hosts at  $z < 1.4$  (refs. <sup>34,35</sup>) (in which  $z < 1.4$  is the upper limit from the UVOT afterglow detections), as well as a galaxy of  $\gtrsim 0.01L^*$  at  $z < 1.4$  (in which  $L^*$  is the characteristic galaxy luminosity parameter<sup>71–75</sup>). The HST limit ( $M_{F_{606W}} \gtrsim -9.9$  mag) also allows us to rule out approximately 46% of the dwarf galaxies that might be associated with SDSS J140910.47+275320.8 (based on Local Group dwarf galaxy luminosities<sup>76</sup>).

## Strong evidence in favour of a $z = 0.076$ origin

Using the Gemini/NIRI image at  $\delta t = 4.1$  days (Fig. 2), we measure an offset of  $5.44'' \pm 0.02''$  ( $7.91 \pm 0.03$  kpc at  $z = 0.076$ ) between the centre of the host galaxy and the position of the optical afterglow. This is within the range of expected offsets from both short and long GRBs, but more consistent with the range for short bursts<sup>35,77–79</sup>.

We note the presence of a second galaxy to the northwest of SDSS J140910.47+275320.8 ('G2' or SDSS J140909.60+275325.8; Fig. 2). Using the Gemini/NIRI image at  $\delta t = 4.1$  days, we measure an offset between the NIR source and G2 of  $10.30'' \pm 0.02''$ . Assuming the spectroscopic redshift for G2 reported in SDSS DR12 (ref. <sup>66</sup>),  $z = 0.4587$ , this is a physical offset of  $60.55 \pm 0.12$  kpc. We measure  $r_{G2} = 20.80 \pm 0.05$  mag from the Binospec template image (see below) and calculate a value of  $P_{cc,G2} = 13.3\%$ . At the spectroscopic redshift of G2, the peak *K*-band luminosity of the counterpart of GRB 211211A is greater than that predicted by kilonova models ( $vL_v = 4 \times 10^{42}$  erg s<sup>-1</sup>). The relatively large  $P_{cc,G2}$  and greater projected and physical offsets in comparison with those of SDSS J140910.47+275320.8 strongly disfavour the potential association between G2 and GRB 211211A.

## Host galaxy observations

On 27 January 2022, we obtained further optical observations in the grz-bands with the Binospec instrument mounted on the MMT<sup>80</sup> (programme no. UAO-G178-21B; Principal Investigator: Rastinejad). We calibrate images to SDSS DR12 and perform aperture photometry on SDSS J140910.47+275320.8 with IRAF/phot. We obtain further host photometry from template observations and the HST images. We retrieve *u*-band photometry of the host from the SDSS archive<sup>66</sup> and W1 photometry from the Wide-field Infrared Survey Explorer (WISE)<sup>81</sup>. We obtain UV photometry from Swift/UVOT (*v*, *b*, *u*, *uvw1*, *uvw2*, *uvm2*, *uvw2* bands). We list all host photometry in Extended Data Tables 1 and 2.

We obtained further spectroscopy of SDSS J140910.47+275320.8 with the DEep Imaging Multi-Object Spectrograph (DEIMOS) mounted

on the 10-m Keck II telescope on 8 January 2022 ( $2 \times 1,500$  s; programme no. O300; Principal Investigator: Blanchard). The spectrum was observed with a 1'' slit and the 600ZD disperser at a central wavelength of 6,500 Å with the GG455 blocking filter, covering the wavelength range of approximately 4,500–9,000 Å. We apply an overscan subtraction, flat-field corrections, model the sky background and remove cosmic rays using Pypelt<sup>82</sup>. We also apply a wavelength calibration with KrXeArNeCdZnHg arc lamp spectra. Using the boxcar method of Pypelt with a 1.5'' radius to encapsulate the light from the entire galaxy, we extract the 1D spectrum from both target science frames. We flux calibrate the spectra with the standard star HZ44, taken the same night as the science target, and co-add the 1D galaxy spectra. Finally, we apply a galactic-extinction correction in the direction of the target using the model of ref. <sup>83</sup> and  $A_{V,\text{ext}}$  from the dust extinction maps of ref. <sup>84</sup>. We confirm the redshift of  $z = 0.0763 \pm 0.0002$  ( $347.8^{+1.0}_{-0.9}$  Mpc) from the identification of the H $\alpha$ , H $\beta$ , [OIII] $\lambda\lambda 4958, 5007$ , [NII] $\lambda\lambda 6549, 6584$  and [SII] $\lambda\lambda 6717, 6731$  emission lines.

## Stellar population modelling of SDSS J140910.47+275320.8

We model the stellar population properties of SDSS J140910.47+275320.8 using Prospector, a Python-based stellar population inference code<sup>85,86</sup>. We determine properties such as the total mass formed ( $M_f$ ), age of the galaxy at the time of observation ( $t_{\text{age}}$ ), optical depth, star formation history (SFH) and stellar ( $Z$ ) and gas-phase ( $Z_{\text{gas}}$ ) metallicities from jointly fitting the photometric and Keck/DEIMOS spectroscopic data at the redshift of the galaxy. We apply a nested sampling fitting routine with DYNESTY<sup>87</sup> to fully sample the parameter space of each property and build model SEDs using FSPS (Flexible Stellar Population Synthesis) and Python-fsp<sup>88,89</sup>. Within the Prospector fit, we use the Milky Way extinction law<sup>83</sup> and assume a Chabrier initial mass function<sup>90</sup>. We apply a parametric delayed- $\tau$  SFH ( $\text{SFH} \propto t \times e^{-t/\tau}$ ), characterized by the e-folding time  $\tau$ , which is a sampled parameter in the Prospector fit. We include the Gallazzi mass–metallicity<sup>91</sup> relation to ensure that Prospector only samples realistic  $M_f$  and  $Z$ -values and enforce a 2:1 dust ratio between old and young stellar populations, as younger stars are observed to attenuate dust twice as much as old stars<sup>85,92</sup>. We build the model spectral continuum from a tenth-order Chebyshev polynomial and model spectral line strengths and widths with a nebular emission model, which includes a gas ionization parameter  $Z_{\text{gas}}$ . We further apply a noise-inflation model to the observed spectrum to ensure proper weighting of the photometry against the high-S/N spectrum. Finally, we convert  $M_f$  to a stellar mass ( $M_*$ ),  $t_{\text{age}}$  to a mass-weighted age ( $t_m$ ) and the optical depth to *V*-band magnitude ( $A_V$ ) using the equations in ref. <sup>93</sup>.

We find that SDSS J140910.47+275320.8 has  $t_m = 4.00^{+0.65}_{-0.59}$  Gyr,  $\log(M_*/M_\odot) = 8.84^{+0.10}_{-0.05}$ ,  $A_V = 0.05^{+0.04}_{-0.03}$  mag,  $\log(Z_*/Z_\odot) = -0.69^{+0.09}_{-0.20}$  and  $\log(Z_{\text{gas}}/Z_\odot) = 0.22^{+0.77}_{-0.34}$ . We show the Prospector SED fit compared with the observed data in Extended Data Fig. 1. We determine an SED SFR using equation (1) in ref. <sup>93</sup> and find that the galaxy has a low SED-inferred SFR =  $0.07 M_\odot \text{ year}^{-1}$  and specific SFR (sSFR)  $\approx 0.10$  Gyr<sup>-1</sup>. Following the methods in refs. <sup>94,95</sup>, we also determine an SFR from the model-predicted emission line flux of H $\alpha$ , finding SFR =  $0.76 \pm 0.01 M_\odot \text{ year}^{-1}$ , which is higher than the SED-inferred SFR. We note that SED-inferred SFRs are typically systematically lower than H $\alpha$ -inferred SFRs<sup>85</sup>. From equation (2) in ref. <sup>96</sup> and using the SED-inferred sSFR and redshift, we determine that the galaxy is star-forming.

Compared with the population of short GRB hosts<sup>29</sup>, SDSS J140910.47+275320.8 lies in approximately the bottom 11.8% of stellar masses, about 86.7% for stellar population age and 19.1% inferred SFR. We note that it has much less star formation for its given stellar mass than other short GRB hosts and is the lowest redshift star-forming host compared with the population<sup>29</sup>. Furthermore, SDSS J140910.47+275320.8 has distinct properties from NGC4993, the quiescent host of GW/GRB170817 (refs. <sup>97–99</sup>). NGC4993 is roughly 9 Gyr older,  $10^2$  times more massive and has much less continuing star formation ( $\approx 10^{-4}$  Gyr<sup>-1</sup> (refs. <sup>29,98</sup>)). Despite these contrasts and considering the low amount of active star

# Article

formation in the host and its old stellar population age, we find little evidence from the host galaxy that GRB 211211A originated in a young massive stellar progenitor.

## Afterglow model

To model the synchrotron afterglow, we use the methods of refs.<sup>19,100,101</sup> (and references therein) and calculate the dynamics of a relativistic blast wave with the analytical solution of ref.<sup>102</sup>. This solution assumes a uniform interstellar medium environment, which is consistent with our results from spectral fitting. We do not find evidence for a reverse shock in the afterglow observations and, thus, model only a forward shock. The eight physical parameters in our model are the inclination between the line of sight and the central axis of the jet ( $i$ ), isotropic equivalent jet kinetic energy ( $E_{\text{K,iso}}$ ), the electron distribution index ( $p$ ), the jet half opening angle ( $\theta_j$ ), the Lorentz factor ( $\Gamma$ ), the circumburst environment density ( $n$ ), the fraction of energy that goes into the magnetic field ( $\varepsilon_B$ ) and the electrons ( $\varepsilon_e$ ). Our model solves for the order of the synchrotron break frequencies resulting from the synchrotron self-absorption ( $\nu_a$ ), electron cooling ( $\nu_c$ ) and the minimum Lorentz factor in the distribution of shocked electrons ( $\nu_m$ ). We constrain the value for  $p$  based on fits to the X-ray data.

We use emcee<sup>103</sup> to determine a best-fit afterglow model and posterior distributions for the physical parameters. We fit our model to the entire X-ray and radio datasets and to the galactic-extinction-corrected UV-optical data at  $\delta t < 0.1$  days, when the synchrotron afterglow luminosity is expected to dominate the kilonova contribution. Overall, our model provides a good fit to the observed data (Fig. 3). We find a slow-cooling spectrum with  $\nu_a < \nu_m < \nu_c$ , in which  $\nu_c$  is above the X-ray frequency and  $\nu_m$  is below the UV-optical frequency. In Extended Data Table 3, we present the median and  $1\sigma$  errors of the physical parameters found by our best-fit model. Early UVOT data constrain the Lorentz factor within our afterglow model to  $\Gamma \approx 70$ , consistent with prompt emission analysis of the burst<sup>104</sup>.

Both our model parameters and the observations are in keeping with those seen in the short GRB population<sup>39</sup>, including GRB 170817A (for example, ref.<sup>105</sup>). The X-ray luminosity of the afterglow on time-scales  $> 1,000$  s lies roughly at the median of short GRB afterglows, whereas the earlier X-ray data are consistent with short GRBs with extended emission<sup>104</sup>. The optical afterglow is also consistent with short GRBs<sup>39</sup>. At later times ( $> 2$  days), our extrapolation is fainter than afterglow detections of some bursts. However, upper limits of numerous other bursts are available at this epoch.

## Kilonova model

We isolate the kilonova light curve by subtracting the median afterglow model from the optical and infrared data, propagating the 1-sigma uncertainties in the afterglow luminosity for each observation into the subtracted data. We fit this afterglow-subtracted photometry to a suite of kilonova models using the prescriptions of refs.<sup>20,21,106</sup> within the Modular Open Source Fitter for Transients (MOSFiT<sup>107</sup>). The luminosity in these models is produced by the radioactive decay of  $r$ -process elements and diffuses out of the ejecta following the standard formalism given by ref.<sup>108</sup>. The ejecta in our models consists of three components produced by different processes in the merger and each has a separate mass, velocity and composition, with more lanthanide-rich material (arising in regions of lower electron fraction and/or neutrino irradiation) having a higher opacity. Although the afterglow model is only fit to  $\gtrsim 3\sigma$  UVOT detections, the kilonova model is fit to UVOT detections at the  $\gtrsim 1\sigma$  level, providing information on the contribution of the shocked cocoon. In Extended Data Table 2, we separately list the photometry used in the afterglow and kilonova modelling.

Interactions between the compact object progenitors produce dynamical ejecta just before and during the merger. ‘Blue’ ( $\kappa = 0.5 \text{ cm}^2 \text{ g}^{-1}$ ) material is ejected in the polar direction and assumed to be lanthanide-free resulting from strong neutrino irradiation, owing to either the

contact shock or surface winds from a magnetar remnant (hence this component is unlikely to exist in a NS–BH merger). Interaction from the jet may also lower the lanthanide fraction of material ejected at the poles<sup>109</sup>. Conversely, ‘red’ ( $\kappa = 10 \text{ cm}^2 \text{ g}^{-1}$ ) dynamical ejecta are produced by tidal tails and are concentrated along the equatorial axis. A post-merger accretion disk formed around the remnant object provides a second source of kilonova ejecta. The amount of material ejected by the disk is dependent on the merger remnant (for example, a prompt-collapse BH or a short-lived NS (for example, ref.<sup>23</sup>)), and can vary by orders of magnitude (in terms of  $M_\odot$ ). The opacity (that is, composition) depends on the exposure to neutrino flux, thought to be higher for a longer-lived NS remnant (such as ref.<sup>110</sup>). Light-curve models for AT 2017gfo suggested that this component had an intermediate ‘purple’ opacity ( $\kappa \approx 3 \text{ cm}^2 \text{ g}^{-1}$ )<sup>20</sup>.

The relative contribution to the total luminosity by each spatially distinct component depends on the observer viewing angle<sup>111</sup>. Given the bright on-axis GRB, we assume a viewing angle along the polar axis of the binary. The luminosity of blue ejecta can be further enhanced by shock heating from the GRB jet traversing the ejecta (such as refs.<sup>112,113</sup>), which we include in our model following ref.<sup>26</sup>. We modify their prescriptions by adding a constraint that shock cooling ceases to contribute luminosity once the cocoon becomes optically thin ( $\lesssim 1$  day; equation (14) in ref.<sup>26</sup>). Our models do not include the effects of jet interaction (such as ref.<sup>109</sup>) or magnetic fields<sup>25,114,115</sup>.

We fit the data using two variations of this model. We adopt flat priors on all parameters in both cases and use DYNESTY<sup>89</sup> to sample the posteriors. We include a white-noise parameter,  $\sigma$ , in the likelihood function as in ref.<sup>107</sup>. First we use a model based on ref.<sup>20</sup> and let the mass  $M_{\text{ej},i}$  and velocity  $v_{\text{ej},i}$  of each ejecta component vary freely. We also include the effects of (fixed) viewing angle and allow the fraction of blue ejecta in the shocked cocoon ( $\zeta_{\text{shock}}$ ) to vary, both following ref.<sup>21</sup>. This model produces the best-fit light curve in Fig. 3. Although the model provides a good fit to the NIR points, it over-predicts the  $i$ -band luminosity for the two detections at  $\delta t \gtrsim 2.5$  days. We note that both of these points have high systematic (precise flux measurements vary up to 1 mag with aperture choice) and statistical (Extended Data Table 1) errors. The posterior distributions of the model parameters are shown in Extended Data Fig. 3. The total model evidence returned by DYNESTY is  $\ln(Z) = 24.9$ . Derived ejecta masses and velocities are, overall, similar to inferences for GW170817 (ref.<sup>20</sup>). The main difference is the ratio of red to purple ejecta, with a larger red mass preferred in GRB 211211A owing to the redder  $-K$  and  $i - K$  colours at about 1 week post-merger.

Although the statistical errors shown in Extended Data Fig. 3 are generally  $\lesssim 10\%$ , the model assumptions of constant grey opacities for each component probably implies a non-negligible systematic error. The opacity is degenerate with ejecta mass and velocity through the light-curve diffusion timescale,  $\tau \propto (\kappa M/v)^{1/2}$ , implying further fractional uncertainty on the  $r$ -process yield up to  $dM/M \approx dk/\kappa \approx 1$ . However, the true systematic error is lower than this because  $M$  is also directly tied to the radioactive heating rate and experiments with freeing the opacities suggest that it is about 50%. In addition, we attempted to fit the data with a two-component model, allowing the opacity of the redder component to vary. In this case, we still recover a total  $r$ -process mass of about  $0.05 M_\odot$ , although the derived opacity ( $2 \text{ cm}^2 \text{ g}^{-1}$ ) and velocity ( $> 0.3c$ ) do not naturally align with an expected ejecta component (see the next section, ‘Binary-based kilonova model’).

To determine whether there are any detectable degeneracies between the afterglow and kilonova posteriors, we perform an approximate joint fit to the data. Adding the kilonova light curves to those of the afterglow during the inference process requires fitting a 15-parameter model. Thus, the Markov chain Monte Carlo samplers naturally struggle to find the global optimum and do not reach convergence in our tests. However, the joint fit does not detect any degeneracies, indicating that the effect of the uncertain afterglow model flux on the kilonova is negligible. The flux contrast between the kilonova and afterglow light

curves also supports this: during the time of the kilonova detections, most epochs have kilonova fluxes one to two orders of magnitude above those of the afterglow. Thus, changes in the afterglow within model uncertainties affect the kilonova only at the few-percent level. At earlier times, when the kilonova is not clearly visible above the afterglow, we have added an earlier Swift/UVOT unfiltered observation to better constrain the early light curve. We find that the resultant changes in the afterglow parameters are small, producing a moderately lower Lorentz factor, with other parameters largely unchanged. This suggests that the afterglow model is robust and that the kilonova is not sensitive to allowed changes in the afterglow.

Because we can find no evidence for strong degeneracies in the models, we have used our two-step approach using the well-tested codes optimized individually for the afterglow and kilonova<sup>19,21</sup>. We propagate all uncertainties in the optical afterglow light curves into the subtracted kilonova photometry before fitting. We also report the afterglow-subtracted photometry in Extended Data Tables 1 and 2.

### Binary-based kilonova model

Advancements in the theoretical modelling of compact object mergers and their outflows have made it possible to tie kilonova observations to properties of the progenitors and remnant (for example, refs. <sup>21,116</sup>). Specifically, the masses of the dynamically ejected, lanthanide-rich red and lanthanide-poor blue components are determined by the progenitor mass ratio ( $q$  (ref. <sup>22</sup>)), chirp mass ( $\mathcal{M}$ ) and NS radius ( $R_{\text{NS}}$ ; for example, ref. <sup>117</sup>). Similarly, an estimate of the intermediate-opacity purple mass ejected by the post-merger accretion disk informs estimates of  $\mathcal{M}, R_{\text{NS}}$  and the NS remnant lifetime (for example, ref. <sup>114</sup>). The ejecta velocities of each component further depend on  $\mathcal{M}$  (ref. <sup>23</sup>). Reformulating the model in terms of pre-merger binary parameters allows greater insight to the progenitor system and ensures that  $M_e - V_{\text{ej}}$  combinations (and, thus, the resulting light curves) are consistent and realistic in the context of theoretical simulations.

We therefore fit the afterglow-subtracted photometry with the binary-based model of ref. <sup>21</sup>. We fix the viewing angle to pole-on and the equation-of-state-dependent parameters to the best-fit values for GW170817:  $R_{\text{NS}} = 11.1 \text{ km}$  and maximum stable mass  $M_{\text{TOV}} = 2.17 M_{\odot}$ . The free parameters are the chirp mass,  $\mathcal{M} = (M_1 M_2)^{3/5} (M_1 + M_2)^{-1/5}$ , and mass ratio,  $q = M_2/M_1 \leq 1$ , in which  $M_1$  and  $M_2$  are the masses of the two neutron stars, the fraction of the remnant disk ejected, the fraction of blue ejecta enhanced by NS surface winds for long-lived remnants and the fraction of blue ejecta shocked by the GRB. We introduce one extra free parameter to the model in ref. <sup>21</sup>: the time after merger at which the GRB jet reheats the polar ejecta (a larger  $t_{\text{shock}}$  results in a brighter cocoon owing to the larger radius of the ejecta). Even if the jet has already broken through the ejecta, recollimation shocks at the jet–ejecta interface may continue to appreciably heat ejecta material as long as the jet is active (for example, ref. <sup>118</sup>), although the efficiency of such heating is probably lower than in the case of a choked jet (for example, ref. <sup>119</sup>). This extra freedom is motivated by the temporally extended GRB duration compared with GRB 170817 and is required to match the early UV emission. The best-fit model is shown in Extended Data Fig. 4, with posteriors shown in Extended Data Fig. 5. The binary masses are  $M_1 = 1.42 \pm 0.05 M_{\odot}$  and  $M_2 = 1.25 \pm 0.04 M_{\odot}$ , consistent with typical NSs (and indeed GW170817). The fraction of disk mass ejected is similar to the approximate value of 0.1 inferred for GW170817 by ref. <sup>21</sup>. We warn that the systematic errors in this model are also around 50% (refs. <sup>21,117</sup>). If a magnetar remnant is the source of the extended emission, we might expect a large value of the blue ejecta enhancement factor ( $1/\alpha$ ) owing to magnetic winds. The mode of the posterior is  $\alpha = 0.6$ , but it is not well constrained owing to a degeneracy with  $q$  visible in Extended Data Fig. 5.

### $^{56}\text{Ni}$ -powered transient model

To further rule out any associated SN, or a white dwarf–NS merger<sup>33</sup>, we also fit the light curve with a single-component model powered

by  $^{56}\text{Ni}$  decay, using the default MOSFiT model. The free parameters in this case are the ejecta mass and velocity, the nickel fraction, the gamma-ray trapping efficiency and a minimum (recombination) temperature. We fixed the optical opacity to  $\kappa = 0.2 \text{ cm}^2 \text{ g}^{-1}$ , appropriate for electron scattering for ionized intermediate mass or iron-group elements. This model is unable to provide a reasonable fit: the model evidence is  $\ln(Z) = -59.6$  because it is too faint by several magnitudes during the first day (Extended Data Fig. 6). Physically, the problem is that a single-component model cannot cool quickly enough to match both the early UV and late-time NIR light curves. The posteriors for velocity ( $\approx 10^5 \text{ km s}^{-1}$ ) and nickel fraction ( $\approx 1$ ) rail against the upper bounds of their priors. This model is therefore heavily disfavoured compared with the kilonova fits.

### Alternative interpretations

The optical-NIR counterpart observed following GRB 211211A is strongly reminiscent of the kilonova AT 2017gfo, and—as our fitting shows—can be explained with a superimposed afterglow and kilonova model. Straightforward dust extinction in the host galaxy or burst vicinity cannot explain the early blue colour of the counterpart and its subsequent evolution from blue to red colours. The measured offset of the optical counterpart of GRB 211211A from the host galaxy centre ( $7.91 \pm 0.03 \text{ kpc}$ ) is highly consistent with the known offsets of short GRBs, which have a median of 7.92 kpc and span about 1.79–28.63 kpc (16th and 84th percentiles<sup>79</sup>). The offset of GRB 211211A is less consistent but still within the range of known long GRB offsets, for which the median is 1.28 kpc and span roughly 0.075–14 kpc (ref. <sup>78</sup>)). The counterpart fades much faster than the rate expected for more distant SN events (for example, a dust-obscured SN at  $z > 0.5$ ). Comparing the  $i$ -band upper limit at  $\delta t = 17.6$  days to the light curves of several long GRB-SNe<sup>3,120–124</sup>, we find that none of the SNe are allowed by our upper limit out to  $z = 0.5$  ( $M > -17.6$ ).

Recently, it has been suggested<sup>125</sup> that the NIR excess of GRB 211211A could instead be caused by an infrared dust echo, a scenario in which dust local to the GRB (such as in a giant molecular cloud) is destroyed by the GRB jet directly along the line of sight and surrounding dust is heated and subsequently reradiates. Direct light-curve modelling is not straightforward for this scenario. Thus one cannot directly compare the dust model to that of a kilonova. We also note that such signatures have not been needed to explain previous long-duration GRB afterglows, although there is a paucity of relevant infrared searches in long GRBs.

The scenario in ref. <sup>125</sup> requires an underlying host fainter than that of all known GRBs at  $z < 3$  (ref. <sup>35</sup>). As the detection of the UVOT afterglow limits the origin of GRB 211211A to  $z < 1.4$ , this explanation requires an extremely faint, low-mass host galaxy unseen so far in the GRB host population<sup>29,35,79</sup>. Because very-low-mass galaxies are typically less dusty than more massive galaxies<sup>126,127</sup>, this is not a probable location to observe a GRB within a dense, dusty environment. We also note that, for a dusty line of sight, we may expect to observe some residual absorption in the form of either excess  $A_V$  or excess X-ray  $N_{\text{H}}$ . We find no evidence for either in the spectrum of GRB 211211A.

One reason that the investigators of ref. <sup>125</sup> prefer the dust echo model over that of a kilonova is based on the observed kilonova colour at 5.1 days. After afterglow subtraction, the flux ratio at this epoch is red, albeit with large uncertainties,  $F_K/F_i = 43 \pm 29$ . This differs from the colours of AT 2017gfo at the same epoch at the approximately 1.2 $\sigma$  level. However, much redder colours at comparable luminosities can be found in other kilonova models, such as the lanthanide-rich models of ref. <sup>128</sup> that were applied to AT 2017gfo. We therefore do not believe that this colour represents a problem for the kilonova interpretation.

Finally, the BAT light curves also show evidence for a short GRB-like origin. We cross-correlate BAT light curves covering the  $t_{90}$  interval in four standard energy channels to measure the delay in the arrival times of soft photons compared with hard photons. In 1-ms time bins, we find delays of  $10 \pm 9 \text{ ms}$  between 15–25-keV and 50–100-keV photons

# Article

(bands 1 and 3), and  $4 \pm 9$  ms between 25–50-keV and 100–150-keV photons (bands 2 and 4). At  $z = 0.076$ , such small spectral lags are consistent with the distribution of short GRBs<sup>28</sup> and inconsistent with the established long GRB lag–luminosity relationship<sup>129,130</sup>. The expected peak luminosity from this relationship ( $\geq 10^{53}$  erg s<sup>-1</sup>) would require  $z \approx 1.5$ , an origin that is disfavoured by our deep HST observations and UVOT afterglow detection.

## GW detection significance

To explore whether the LIGO/Virgo network (H1, L1 and V1) could have detected the merger precipitating GRB 211211A had it been operating at the time, we consider two representative cases for the progenitors: a  $1.4 + 1.4 M_{\odot}$  BNS merger and a  $1.4 + 5.0 M_{\odot}$  NS–BH merger viewed face on ( $\theta_{jn} = 0$ ). Our calculations use a 2,048-s-duration data segment (chosen to be long enough even for a binary neutron star starting at 10 Hz) with a similarly high sampling frequency of 8,192 Hz. We take the frequency integral between  $f_{\text{low}} = 10$  Hz or 20 Hz and  $f_{\text{high}} = 4,000$  Hz and neglect component spins, orbital eccentricity and tidal effects. Although these parameters will affect the binary phasing, we expect them to have a very small effect on the S/N. We also neglect all cosmological effects and set the phase and polarizations angles to zero, as they will have negligible effect on the S/N. We use the waveform IMRPhenomPv2 NRTidal<sup>131–133</sup> called through BILBY<sup>134,135</sup> and obtain the noise power spectral densities (actual and predicted) from <https://dcc.ligo.org/LIGO-T2000012/public>.

For both the BNS and NS–BH mergers, we consider four representative cases: with  $f_{\text{low}} = 20$  Hz, the O3 (actual), O4 and O5 (predicted) noise curves and O5 with a more optimistic low-frequency cutoff of  $f_{\text{low}} = 10$  Hz. We calculate all S/N using  $D_L = 350$  Mpc, the time of the burst and the coordinates of the XRT position of GRB 211211A. We find that the BNS would not be detectable in O3 ( $S/N \approx 7.4$ ) but the NS–BH would have been ( $S/N \approx 11.7$ ). The BNS and the NS–BH would have had  $S/N > 10$  in O4 and O5, probably making them detectable in GWs.

## Comparison with AT 2017gfo and short GRB kilonova candidates

Despite accompanying an event that is superlative in numerous ways, the kilonova of GRB 211211A is unremarkable in luminosity and colour compared with its few peers. In Extended Data Fig. 7, we plot *i*-band and *K*-band light curves of the kilonova of GRB 211211A, along with the light curve of AT 2017gfo<sup>9–12,14,20,106,112,136–146</sup> and relevant rest-frame short GRB observations from the catalogue of ref. <sup>147</sup>. Owing to the limits of current NIR detectors, we are only able to compare the rest-frame *K*-band light curve of GRB 211211A with that of AT 2017gfo, although we include rest-frame *J/H*-band short GRB kilonova observations for context (open symbols). At  $\delta t \approx 5.1$  days, the only epoch of concurrent *i*-band and *K*-band detections of GRB 211211A, we measure a colour of  $(i - K) = 3.6$  mags. This is redder than the  $(i - K) = 2.0$  mags measured at a similar rest-frame epoch for AT 2017gfo<sup>20</sup>.

In Extended Data Fig. 8, we plot the best-fit ejecta and mass velocity estimates for GRB 211211A compared with those of AT 2017gfo (red boxes; compiled in ref. <sup>148</sup> and references therein) and short GRB kilonova candidates<sup>105,149,150</sup>. Our estimates for GRB 211211A are compatible with those of past kilonovae, including AT 2017gfo. Estimates are highly model-dependent and, thus, direct comparisons are not advisable.

## Reporting summary

Further information on research design is available in the Nature Portfolio Reporting Summary linked to this article.

## Data availability

Most of the data generated or analysed during this study are included in the Extended Data Tables of this article. Gamma-ray and X-ray light curves may be downloaded from the UK Swift Science Data Centre and the online HEASARC archive at <https://heasarc.gsfc.nasa.gov/W3Browse/fermi/fermigbrst.html>. Any further data requests should be made to J.C.R.

## Code availability

The kilonova model scripts are available at <https://github.com/guillochon/MOSFiT>. The scripts used to model the afterglow will be publicly available on publication of this manuscript. The Prospector stellar population modelling code is available at <https://github.com/bd-j/prospector>.

41. Bennett, C. L., Larson, D., Weiland, J. L. & Hinshaw, G. The 1% concordance Hubble constant. *Astrophys. J.* **794**, 135 (2014).
42. Meegan, C. et al. The Fermi gamma-ray burst monitor. *Astrophys. J.* **702**, 791–804 (2009).
43. Adriani, O. et al. Extended measurement of the cosmic-ray electron and positron spectrum from 11 GeV to 4.8 TeV with the calorimetric electron telescope on the International Space Station. *Phys. Rev. Lett.* **120**, 261102 (2018).
44. Tamura, T. et al. GRB 211211A: CALET Gamma-Ray Burst Monitor detection. GRB Coordinates Network, Circular Service, No. 31226 (2021).
45. Vedrenne, G. et al. SPI: the spectrometer aboard INTEGRAL. *Astron. Astrophys.* **411**, 63–70 (2003).
46. Minaev, P. & Pozanenko, A.; GRB IKI FuN. GRB 211211A: redshift estimation and SPI-ACS/INTEGRAL detection. GRB Coordinates Network, Circular Service, No. 31230 (2021).
47. Burrows, D. N. et al. The Swift X-ray telescope. *Space Sci. Rev.* **120**, 165–195 (2005).
48. Evans, P. A. et al. An online repository of *Swift*/XRT light curves of γ-ray bursts. *Astron. Astrophys.* **469**, 379–385 (2007).
49. Evans, P. A. et al. Methods and results of an automatic analysis of a complete sample of Swift-XRT observations of GRBs. *Mon. Not. R. Astron. Soc.* **397**, 1177–1201 (2009).
50. Gehrels, N. et al. Correlations of prompt and afterglow emission in *Swift* long and short gamma-ray bursts. *Astrophys. J.* **689**, 1161–1172 (2008).
51. Poole, T. S. et al. Photometric calibration of the *Swift* ultraviolet/optical telescope. *Mon. Not. R. Astron. Soc.* **383**, 627–645 (2008).
52. Breeveld, A. A. et al. An updated ultraviolet calibration for the *Swift*/UVOT. *AIP Conf. Proc.* **1358**, 373–376 (2011).
53. McMullin, J. P., Waters, B., Schiebel, D., Young, W. & Golap, K. CASA architecture and applications. *ASP Conf. Ser.* **376**, 127–130 (2007).
54. Malesani, D. B. et al. GRB 211211A: NOT optical spectroscopy. GRB Coordinates Network, Circular Service, No. 31221 (2021).
55. Chambers, K. C. et al. The Pan-STARRS1 Surveys. Preprint at <https://arxiv.org/abs/1612.05560> (2016).
56. Tody, D. IRAF in the nineties. *ASP Conf. Ser.* **52**, 173–183 (1993).
57. Hodapp, K. W. et al. The Gemini Near-Infrared Imager (NIRI). *Publ. Astron. Soc. Pac.* **115**, 1388–1406 (2003).
58. Hook, I. M. et al. The Gemini–North Multi-Object Spectrograph: performance in imaging, long-slit, and multi-object spectroscopic modes. *Publ. Astron. Soc. Pac.* **116**, 425–440 (2004).
59. McLeod, B. et al. MMT and Magellan infrared spectrograph. *Publ. Astron. Soc. Pac.* **124**, 1318 (2012).
60. Labrie, K., Anderson, K., Cárdenas, R., Simpson, C. & Turner, J. E. H. DRAGONS - Data Reduction for Astronomy from Gemini Observatory North and South. *ASP Conf. Ser.* **523**, 321 (2019).
61. Paterson, K. POTPyRI: Pipeline for Optical/infrared Telescopes in Python for Reducing Images. <https://github.com/CIERA-Transients/POTPyRI/>.
62. Lang, D., Hogg, D. W., Mierle, K., Blanton, M. & Roweis, S. Astrometry.net: blind astrometric calibration of arbitrary astronomical images. *Astron. J.* **139**, 1782–1800 (2010).
63. Seifert, W. et al. LUCIFER: a multimode NIR instrument for the LBT. *Proc. SPIE* **4841**, 962–973 (2003).
64. Fontana, A. et al. The Hawk-I UDS and GOODS Survey (HUGS): survey design and deep K-band number counts. *Astron. Astrophys.* **570**, A11 (2014).
65. Becker, A. HOTPANTS: High Order Transform of PSF ANd Template Subtraction. Astrophysics Source Code Library, record ascl:1504.004 (2015).
66. Alam, S. et al. The eleventh and twelfth data releases of the Sloan Digital Sky Survey: final data from SDSS-III. *Astrophys. J. Suppl. Ser.* **219**, 12 (2015).
67. Skrutskie, M. F. et al. The Two Micron All Sky Survey (2MASS). *Astron. J.* **131**, 1163–1183 (2006).
68. Kilpatrick, C. D. hst123. <https://github.com/charliekilpatrick/hst123>.
69. Kilpatrick, C. D. et al. Hubble Space Telescope observations of GW170817: complete light curves and the properties of the galaxy merger of NGC 4993. *Astrophys. J.* **926**, 49 (2022).
70. Dolphin, A. DOLPHOT: stellar photometry. Astrophysics Source Code Library, record ascl:1608.013 (2016).
71. Brown, W. R., Geller, M. J., Fabricant, D. G. & Kurtz, M. J. V- and R-band galaxy luminosity functions and low surface brightness galaxies in the century survey. *Astron. J.* **122**, 714–728 (2001).
72. Wolf, C. et al. The COMBO-17 survey: evolution of the galaxy luminosity function from 25 000 galaxies with  $0.2 < z < 1.2$ . *Astron. Astrophys.* **401**, 73–98 (2003).
73. Willmer, C. N. A. et al. The Deep Evolutionary Exploratory Probe 2 galaxy redshift survey: the galaxy luminosity function to  $z \sim 1$ . *Astrophys. J.* **647**, 853–873 (2006).
74. Reddy, N. A. & Steidel, C. C. A steep faint-end slope of the UV luminosity function at  $z \sim 2$ –3: implications for the global stellar mass density and star formation in low-mass halos. *Astrophys. J.* **692**, 778–803 (2009).
75. Finkelstein, S. L. et al. The evolution of the galaxy rest-frame ultraviolet luminosity function over the first two billion years. *Astrophys. J.* **810**, 71 (2015).

76. McConnachie, A. W. The observed properties of dwarf galaxies in and around the Local Group. *Astron. J.* **144**, 4 (2012).
77. Fong, W. F. & Berger, E. The locations of short gamma-ray bursts as evidence for compact object binary progenitors. *Astrophys. J.* **776**, 18 (2013).
78. Blanchard, P. K., Berger, E. & Fong, W.-f. The offset and host light distributions of long gamma-ray bursts: a new view from HST observations of Swift bursts. *Astrophys. J.* **817**, 144 (2016).
79. Fong, W.-f. et al. Short GRB host galaxies I: photometric and spectroscopic catalogs, host associations, and galactocentric offsets. Preprint at <https://arxiv.org/abs/2206.01763> (2022).
80. Fabricant, D. et al. Binospec: a wide-field imaging spectrograph for the MMT. *Publ. Astron. Soc. Pac.* **131**, 075004 (2019).
81. Wright, E. L. et al. The Wide-field Infrared Survey Explorer (WISE): mission description and initial on-orbit performance. *Astron. J.* **140**, 1868–1881 (2010).
82. Prochaska, J. et al. PyPelt: the Python spectroscopic data reduction pipeline. *J. Open Source Softw.* **5**, 2308 (2020).
83. Cardelli, J. A., Clayton, G. C. & Mathis, J. S. The relationship between infrared, optical, and ultraviolet extinction. *Astrophys. J.* **345**, 245 (1989).
84. Schlafly, E. F. & Finkbeiner, D. P. Measuring reddening with Sloan Digital Sky Survey stellar spectra and recalibrating SFD. *Astrophys. J.* **737**, 103 (2011).
85. Leja, J. et al. An older, more quiescent universe from panchromatic SED fitting of the HST-HST survey. *Astrophys. J.* **877**, 140 (2019).
86. Johnson, B. D., Leja, J., Conroy, C. & Speagle, J. S. Stellar population inference with prospector. *Astrophys. J. Suppl. Ser.* **254**, 22 (2021).
87. Speagle, J. S. DYNESTY: a dynamic nested sampling package for estimating Bayesian posteriors and evidences. *Mon. Not. R. Astron. Soc.* **493**, 3132–3158 (2020).
88. Conroy, C., Gunn, J. E. & White, M. The propagation of uncertainties in stellar population synthesis modeling. I. The relevance of uncertain aspects of stellar evolution and the initial mass function to the derived physical properties of galaxies. *Astrophys. J.* **699**, 486–506 (2009).
89. Conroy, C. & Gunn, J. E. The propagation of uncertainties in stellar population synthesis modeling. III. Model calibration, comparison, and evaluation. *Astrophys. J.* **712**, 833–857 (2010).
90. Chabrier, G. Galactic stellar and substellar initial mass function. *Publ. Astron. Soc. Pac.* **115**, 763–795 (2003).
91. Gallazzi, A., Charlot, S., Brinchmann, J., White, S. D. M. & Tremonti, C. A. The ages and metallicities of galaxies in the local universe. *Mon. Not. R. Astron. Soc.* **362**, 41–58 (2005).
92. Calzetti, D. et al. The dust content and opacity of actively star-forming galaxies. *Astrophys. J.* **533**, 682–695 (2000).
93. Nugent, A. E. et al. The distant, galaxy cluster environment of the short GRB 161104A at  $z \sim 0.8$  and a comparison to the short GRB host population. *Astrophys. J.* **904**, 52 (2020).
94. Kennicutt, J. & Robert, C. Star formation in galaxies along the Hubble sequence. *Annu. Rev. Astron. Astrophys.* **36**, 189–232 (1998).
95. Moustakas, J., Kennicutt, J., Robert, C. & Tremonti, C. A. Optical star formation rate indicators. *Astrophys. J.* **642**, 775–796 (2006).
96. Tacchella, S. et al. Fast, slow, early, late: quenching massive galaxies at  $z \sim 0.8$ . *Astrophys. J.* **926**, 134.
97. Abbott, B. P. et al. GW170817: observation of gravitational waves from a binary neutron star inspiral. *Phys. Rev. Lett.* **119**, 161101 (2017).
98. Blanchard, P. K. et al. The electromagnetic counterpart of the binary neutron star merger LIGO/Virgo GW170817. VII. Properties of the host galaxy and constraints on the merger timescale. *Astrophys. J.* **848**, L22 (2017).
99. Levan, A. J. et al. The environment of the binary neutron star merger GW170817. *Astrophys. J.* **848**, L28 (2017).
100. Lamb, G. P. & Kobayashi, S. Electromagnetic counterparts to structured jets from gravitational wave detected mergers. *Mon. Not. R. Astron. Soc.* **472**, 4953–4964 (2017).
101. Lamb, G. P., Mandel, I. & Resmi, L. Late-time evolution of afterglows from off-axis neutron star mergers. *Mon. Not. R. Astron. Soc.* **481**, 2581–2589 (2018).
102. Pe'er, A. Dynamical model of an expanding shell. *Astrophys. J.* **752**, L8 (2012).
103. Foreman-Mackey, D., Hogg, D. W., Lang, D. & Goodman, J. emcee: the MCMC hammer. *Publ. Astron. Soc. Pac.* **125**, 306 (2013).
104. Gompertz, B. P. et al. A minute-long merger-driven gamma-ray burst from fast-cooling synchrotron emission. *Nat. Astron.* <https://doi.org/10.1038/s41550-022-01819-4> (2022).
105. Lamb, G. P. et al. Short GRB 160821B: a reverse shock, a refreshed shock, and a well-sampled kilonova. *Astrophys. J.* **883**, 48 (2019).
106. Cowperthwaite, P. S. et al. The electromagnetic counterpart of the binary neutron star merger LIGO/Virgo GW170817. II. UV, optical, and near-infrared light curves and comparison to kilonova models. *Astrophys. J.* **848**, L17 (2017).
107. Guillotin-Plantier, J. et al. MOSFIT: modular open source fitter for transients. *Astrophys. J. Suppl. Ser.* **236**, 6 (2018).
108. Arnett, W. D. Type I supernovae. I. Analytic solutions for the early part of the light curve. *Astrophys. J.* **253**, 785–797 (1982).
109. Nativi, L. et al. Can jets make the radioactively powered emission from neutron star mergers bluer? *Mon. Not. R. Astron. Soc.* **500**, 1772–1783 (2021).
110. Lippuner, J. & et al. Signatures of hypermassive neutron star lifetimes on r-process nucleosynthesis in the disc ejecta from neutron star mergers. *Mon. Not. R. Astron. Soc.* **472**, 904–918 (2017).
111. Darbha, S. & Kasen, D. Inclination dependence of kilonova light curves from globally aspherical geometries. *Astrophys. J.* **897**, 150 (2020).
112. Kasliwal, M. M. et al. Illuminating gravitational waves: a concordant picture of photons from a neutron star merger. *Science* **358**, 1559–1565 (2017).
113. Arcavi, I. The first hours of the GW170817 kilonova and the importance of early optical and ultraviolet observations for constraining emission models. *Astrophys. J.* **855**, 23 (2018).
114. Radice, D., Perego, A., Bernuzzi, S. & Zhang, B. Long-lived remnants from binary neutron star mergers. *Mon. Not. R. Astron. Soc.* **481**, 3670–3682 (2018).
115. Ciolfi, R. & Kalinani, J. V. Magnetically driven baryon winds from binary neutron star merger remnants and the blue kilonova of 2017 August. *Astrophys. J.* **900**, L35 (2020).
116. Coughlin, M. W., Dietrich, T., Margalit, B. & Metzger, B. D. Multimessenger Bayesian parameter inference of a binary neutron star merger. *Mon. Not. R. Astron. Soc.* **489**, 91–96 (2019).
117. Dietrich, T. & Ujevic, M. Modeling dynamical ejecta from binary neutron star mergers and implications for electromagnetic counterparts. *Class. Quantum Gravity* **34**, 105014 (2017).
118. Gottlieb, O., Bromberg, O., Singh, C. B. & Nakar, E. The structure of weakly magnetized y-ray burst jets. *Mon. Not. R. Astron. Soc.* **498**, 3320–3333 (2020).
119. Duffell, P. C., Quataert, E., Kasen, D. & Klion, H. Jet dynamics in compact object mergers: GW170817 likely had a successful jet. *Astrophys. J.* **866**, 3 (2018).
120. Matheson, T. et al. Photometry and spectroscopy of GRB 030329 and its associated supernova 2003dh: the first two months. *Astrophys. J.* **599**, 394–407 (2003).
121. Clocchiatti, A., Sunzeff, N. B., Covarrubias, R. & Candia, P. The ultimate light curve of SN 1998bw/GRB 980425. *Astron. J.* **141**, 163 (2011).
122. Cano, Z. et al. A trio of gamma-ray burst supernovae: GRB 120729A, GRB 130215A/SN 2013ez, and GRB 130831A/SN 2013fu. *Astron. Astrophys.* **568**, A9 (2014).
123. Greiner, J. et al. A very luminous magnetar-powered supernova associated with an ultra-long y-ray burst. *Nature* **523**, 189–192 (2015).
124. Cano, Z. et al. GRB 161219B/SN 2016jca: a low-redshift gamma-ray burst supernova powered by radioactive heating. *Astron. Astrophys.* **605**, A107 (2017).
125. Waxman, E., Ofek, E. O. & Kushnir, D. Strong NIR emission following the long duration GRB 211211A: dust heating as an alternative to a kilonova. Preprint at <https://arxiv.org/abs/2206.10710> (2022).
126. Santini, P. et al. The evolution of the dust and gas content in galaxies. *Astron. Astrophys.* **562**, A30 (2014).
127. Calura, F. et al. The dust-to-stellar mass ratio as a valuable tool to probe the evolution of local and distant star-forming galaxies. *Mon. Not. R. Astron. Soc.* **465**, 54–67 (2017).
128. Kasen, D., Metzger, B., Barnes, J., Quataert, E. & Ramirez-Ruiz, E. Origin of the heavy elements in binary neutron-star mergers from a gravitational-wave event. *Nature* **551**, 80–84 (2017).
129. Ukwatta, T. N. et al. Spectral lags and the lag-luminosity relation: an investigation with Swift BAT gamma-ray bursts. *Astrophys. J.* **711**, 1073–1086 (2010).
130. Ukwatta, T. N. et al. The lag-luminosity relation in the GRB source frame: an investigation with Swift BAT bursts. *Mon. Not. R. Astron. Soc.* **419**, 614–623 (2012).
131. Hannam, M. et al. Simple model of complete precessing black-hole-binary gravitational waveforms. *Phys. Rev. Lett.* **113**, 151101 (2014).
132. Khan, S. et al. Frequency-domain gravitational waves from nonprecessing black-hole binaries. II. A phenomenological model for the advanced detector era. *Phys. Rev. D* **93**, 044007 (2016).
133. Dietrich, T., Bernuzzi, S. & Tichy, W. Closed-form tidal approximants for binary neutron star gravitational waveforms constructed from high-resolution numerical relativity simulations. *Phys. Rev. D* **96**, 121501 (2017).
134. Ashton, G. et al. Bilby: a user-friendly Bayesian inference library for gravitational-wave astronomy. *Astrophys. J. Suppl. Ser.* **241**, 27 (2019).
135. LIGO Scientific Collaboration. LIGO Algorithm Library - LALSuite. free software (GPL) (2018).
136. Andreoni, I. et al. Follow up of GW170817 and its electromagnetic counterpart by Australian-led observing programmes. *Publ. Astron. Soc. Aust.* **34**, e069 (2017).
137. Diaz, M. C. et al. Observations of the first electromagnetic counterpart to a gravitational-wave source by the TOROS collaboration. *Astrophys. J.* **848**, L29 (2017).
138. Drout, M. R. et al. Light curves of the neutron star merger GW170817/SSS17a: implications for r-process nucleosynthesis. *Science* **358**, 1570–1574 (2017).
139. Evans, P. A. et al. Swift and NuSTAR observations of GW170817: detection of a blue kilonova. *Science* **358**, 1565–1570 (2017).
140. Hu, L. et al. Optical observations of LIGO source GW 170817 by the Antarctic Survey Telescopes at Dome A, Antarctica. *Sci. Bull.* **62**, 1433–1438 (2017).
141. Pian, E. et al. Spectroscopic identification of r-process nucleosynthesis in a double neutron-star merger. *Nature* **551**, 67–70 (2017).
142. Pozanenko, A. S. et al. GRB 170817A associated with GW170817: multi-frequency observations and modeling of prompt gamma-ray emission. *Astrophys. J.* **852**, L30 (2018).
143. Shappee, B. J. et al. Early spectra of the gravitational wave source GW170817: evolution of a neutron star merger. *Science* **358**, 1574–1578 (2017).
144. Smartt, S. J. et al. A kilonova as the electromagnetic counterpart to a gravitational-wave source. *Nature* **551**, 75–79 (2017).
145. Troja, E. et al. The X-ray counterpart to the gravitational-wave event GW170817. *Nature* **551**, 71–74 (2017).
146. Utsumi, Y. et al. J-GEM observations of an electromagnetic counterpart to the neutron star merger GW170817. *Publ. Astron. Soc. Jpn.* **69**, 101 (2017).
147. Rastinejad, J. C. et al. Probing kilonova ejecta properties using a catalog of short gamma-ray burst observations. *Astrophys. J.* **916**, 89 (2021).
148. Siegel, D. M. GW170817—the first observed neutron star merger and its kilonova: implications for the astrophysical site of the r-process. *Eur. Phys. J. A* **55**, 203 (2019).
149. Barnes, J., Kasen, D., Wu, M.-R. & Martinez-Pinedo, G. Radioactivity and thermalization in the ejecta of compact object mergers and their impact on kilonova light curves. *Astrophys. J.* **829**, 110 (2016).
150. Troja, E. et al. The afterglow and kilonova of the short GRB 160821B. *Mon. Not. R. Astron. Soc.* **489**, 2104–2116 (2019).
151. Fong, W. et al. The broadband counterpart of the short GRB 200522A at  $z = 0.5536$ : a luminous kilonova or a collimated outflow with a reverse shock? *Astrophys. J.* **906**, 127 (2021).
152. Fox, D. B. et al. The afterglow of GRB 050709 and the nature of the short-hard y-ray bursts. *Nature* **437**, 845–850 (2005).
153. Berger, E., Fong, W. & Chornock, R. An r-process kilonova associated with the short-hard GRB 130603B. *Astrophys. J.* **774**, L23 (2013).
154. Tanvir, N. R. et al. A ‘kilonova’ associated with the short-duration y-ray burst GRB 130603B. *Nature* **500**, 547–549 (2013).

# Article

155. O'Connor, B. et al. A tale of two mergers: constraints on kilonova detection in two short GRBs at  $z \sim 0.5$ . *Mon. Not. R. Astron. Soc.* **502**, 1279–1298 (2021).
156. Ito, N. et al. GRB 211211A: MITSuME Akeno optical observation. GRB Coordinates Network, Circular Service, No. 31217 (2021).
157. Xiao, S. et al. The quasi-periodically oscillating precursor of a long gamma-ray burst from a binary neutron star merger. Preprint at <https://arxiv.org/abs/2205.02186> (2022).
158. Kumar, H. et al. GRB 211211A: HCT and GIT optical follow up observations. GRB Coordinates Network, Circular Service, No. 31227 (2021).
159. Strausbaugh, R. & Cucchiara, A. GRB 211211A: LCO optical observations. GRB Coordinates Network, Circular Service, No. 31214 (2021).
160. Mao, J., Xin, Y.-X. & Bai, J.-M. GRB 211211A: GMG upper limit. GRB Coordinates Network, Circular Service, No. 31232 (2021).
161. Gupta, R. et al. GRB 211211A: observations with the 3.6m Devasthal Optical Telescope. GRB Coordinates Network, Circular Service, No. 31299 (2021).
162. Moskvitin, A., Spiridonova, O., Belkin, S., Pozanenko, A. & Pankov, N.; GRB IKI FuN. GRB 211211A: SAO RAS optical observations. GRB Coordinates Network, Circular Service, No. 31234 (2021).
163. Mei, A. et al. GeV emission from a compact binary merger. *Nature* <https://doi.org/10.1038/s41586-022-05350-5404-7> (2022).

**Acknowledgements** We thank S. Kattner, S. Self, J. Hinz and I. Chilingarian at the MMT and J. Andrews and K. Chiboucas at Gemini Observatory for their assistance in obtaining observations. We thank A. von Kienlin for providing the GBM hardness versus duration data. We thank P. Schmidt and G. Pratter for assistance with the LIGO S/R calculations. The Fong group at Northwestern acknowledges support by the National Science Foundation under grant nos. AST-1814782 and AST-1909358 and CAREER grant no. AST-2047919. W.F. gratefully acknowledges support by the David and Lucile Packard Foundation. A.J.L. and D.B.M. are supported by the European Research Council (ERC) under the European Union's Horizon 2020 research and innovation programme (grant agreement no. 725246). M.N. and B.P.G. are supported by the ERC under the European Union's Horizon 2020 research and innovation programme (grant agreement no. 948381). M.N. acknowledges a Turing Fellowship. G.P.L. is supported by the UK Science and Technology Facilities Council grant ST/S000453/1. A.R. and E.M. acknowledge support from the INAF research project 'LBT - Supporto Arizona Italia'. J.F.A.F. acknowledges support from the Spanish Ministerio de Ciencia, Innovación y Universidades through the grant PRE2018-086507. D.A.K. and J.F.A.F. acknowledge support from Spanish National Research Project RTI2018-098104-J-I00 (GRBPhot). W. M. Keck Observatory and MMT Observatory access was supported by Northwestern University and the Center for Interdisciplinary Exploration and Research in Astrophysics (CIERA). Some of the data presented herein were obtained at the W. M. Keck Observatory, which is operated as a scientific partnership among the California Institute of Technology, the University of California and the National Aeronautics and Space Administration (NASA). The Observatory was made possible by the generous financial support of the W. M. Keck Foundation. We wish to recognize and acknowledge the very important cultural role and reverence that the summit of Maunakea has always had within the indigenous Hawaiian community. We are most fortunate to have the opportunity to conduct observations from this mountain. Observations reported here were obtained at the MMT Observatory, a joint facility of the University of Arizona and the Smithsonian Institution. On the basis of observations obtained at the international Gemini Observatory (programme ID GN2021B-Q-109), a programme of NOIRLab, which is managed by the Association of Universities for Research in Astronomy (AURA) under a cooperative agreement with the National Science Foundation on behalf of the Gemini Observatory partnership: the National Science Foundation (United States), National Research Council (Canada), Agencia Nacional de Investigación y Desarrollo (Chile), Ministerio de Ciencia, Tecnología e Innovación (Argentina), Ministério da Ciência, Tecnologia, Inovações e Comunicações (Brazil) and Korea Astronomy and Space Science Institute (Republic of Korea).

Processed using the Gemini IRAF package and DRAGONS (Data Reduction for Astronomy from Gemini Observatory North and South). This work made use of data supplied by the UK Swift Science Data Centre at the University of Leicester. The National Radio Astronomy Observatory is a facility of the National Science Foundation operated under cooperative agreement by Associated Universities, Inc. This research is based on observations made with the NASA/ESA Hubble Space Telescope obtained from the Space Telescope Science Institute, which is operated by the AURA, Inc., under NASA contract NAS 5-26555. These observations are associated with programme no. 16923. This work is partly based on observations made with the Gran Telescopio Canarias, installed at the Spanish Observatorio del Roque de los Muchachos of the Instituto de Astrofísica de Canarias, on the island of La Palma. Partly based on observations collected at the Calar Alto Astronomical Observatory, operated jointly by Instituto de Astrofísica de Andalucía (CSIC) and Junta de Andalucía. Partly based on observations made with the Nordic Optical Telescope, under programme 64-502, owned in collaboration by the University of Turku and Aarhus University, and operated jointly by Aarhus University, the University of Turku and the University of Oslo, representing Denmark, Finland and Norway, respectively, the University of Iceland and Stockholm University at the Observatorio del Roque de los Muchachos, La Palma, Spain, of the Instituto de Astrofísica de Canarias. The LBT is an international collaboration among institutions in the United States, Italy and Germany. LBT Corporation partners are: The University of Arizona on behalf of the Arizona Board of Regents; Istituto Nazionale di Astrofisica, Italy; LBT Beteiligungsgesellschaft, Germany, representing the Max Planck Society; The Leibniz Institute for Astrophysics Potsdam and Heidelberg University; The Ohio State University, representing OSU, University of Notre Dame, University of Minnesota and University of Virginia.

**Author contributions** J.C.R. is Principal Investigator of the MMT observations (shared Principal Investigator with N.S. on MMIRS follow-up) and the HST programme. J.C.R. reduced and analysed most of the optical-NIR data and led the writing. B.P.G. identified the source as a possible merger, analysed the high-energy observations, provided modelling support and contributed to the text. A.J.L. analysed observations, provided analysis and co-wrote the text. W.F. is Principal Investigator of the Gemini and VLA programmes and provided input on analysis and text. M.N. performed the kilonova and the Ni-powered transient modelling, and contributed text. G.P.L. identified the source as a possible merger, devised the joint kilonova and afterglow modelling method, and modelled the afterglow. D.B.M. is Principal Investigator of the NOT follow-up, and reduced and analysed observations. A.E.N. reduced the Keck spectrum and performed stellar population modelling. S.R.O. analysed the Swift/JVOT observations. N.R.T. provided input and rates analysis. A.d.U.P., D.A.K., J.F.A.F. and C.C.T. executed and reduced the CAHA and GTC observations. C.D.K. reduced and analysed the HST observations. C.J.M. calculated the GW observability. B.D.M., R.C. and M.E.R. provided input on modelling and analysis. A.R. and E.M. executed and reduced the LBT observation. G.S. executed and reduced the radio observation. J.J., D.J.S. and N.S. contributed MMT follow-up time and provided input on the scientific interpretation. L.I. and J.P.U.F. contributed to reduction of the NOT observations. A.E.N., P.K.B., C.D.K. and H.M.S. executed the Keck spectrum. E.B., R.C., B.E.C., M.D.P., T.L., K.P. and A.R.E. are co-investigators of the programmes used in this work and/or provided input on the scientific interpretation.

**Competing interests** The authors declare no competing interests.

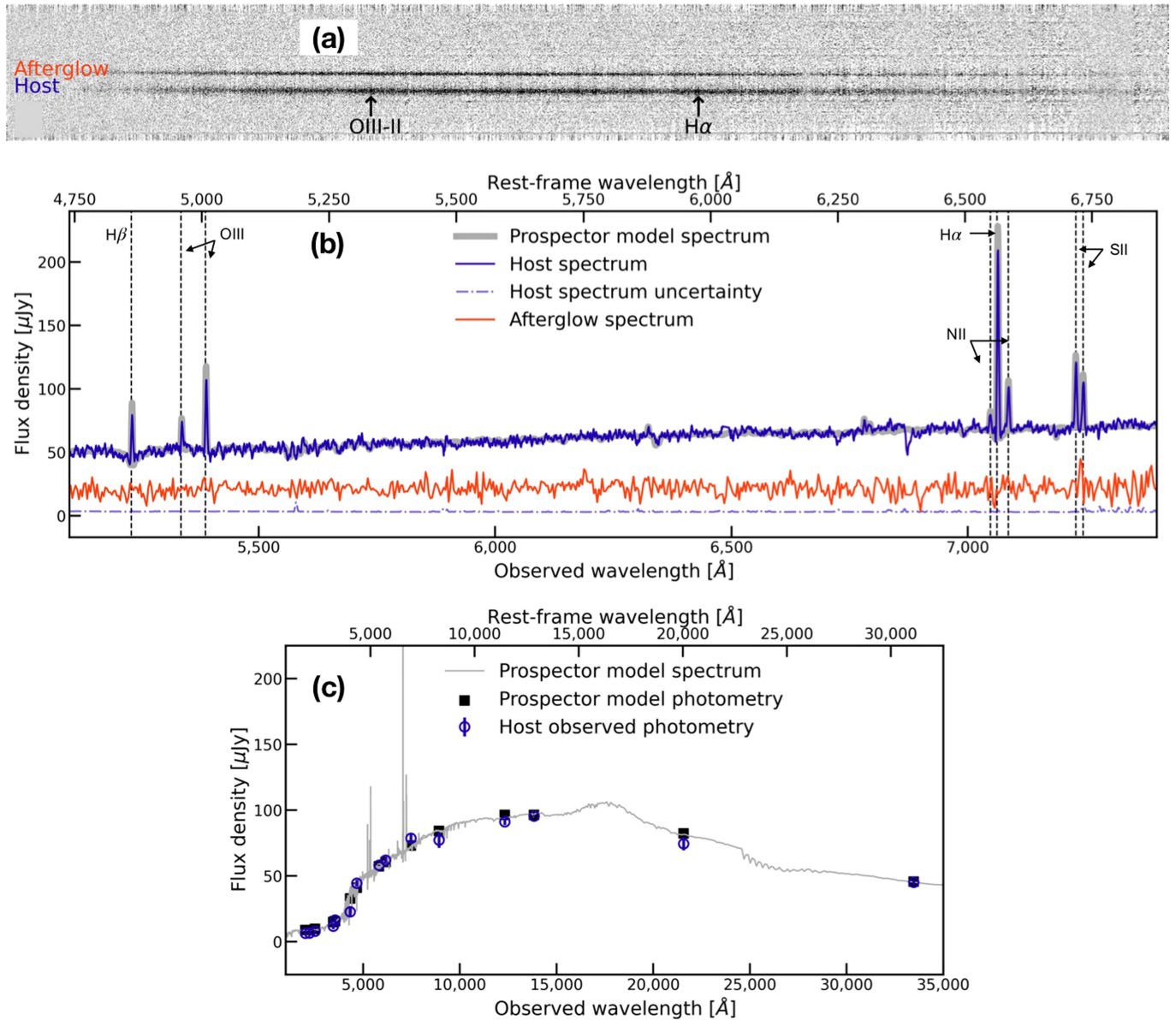
## Additional information

**Supplementary information** The online version contains supplementary material available at <https://doi.org/10.1038/s41586-022-05390-w>.

**Correspondence and requests for materials** should be addressed to Jillian C. Rastinejad.

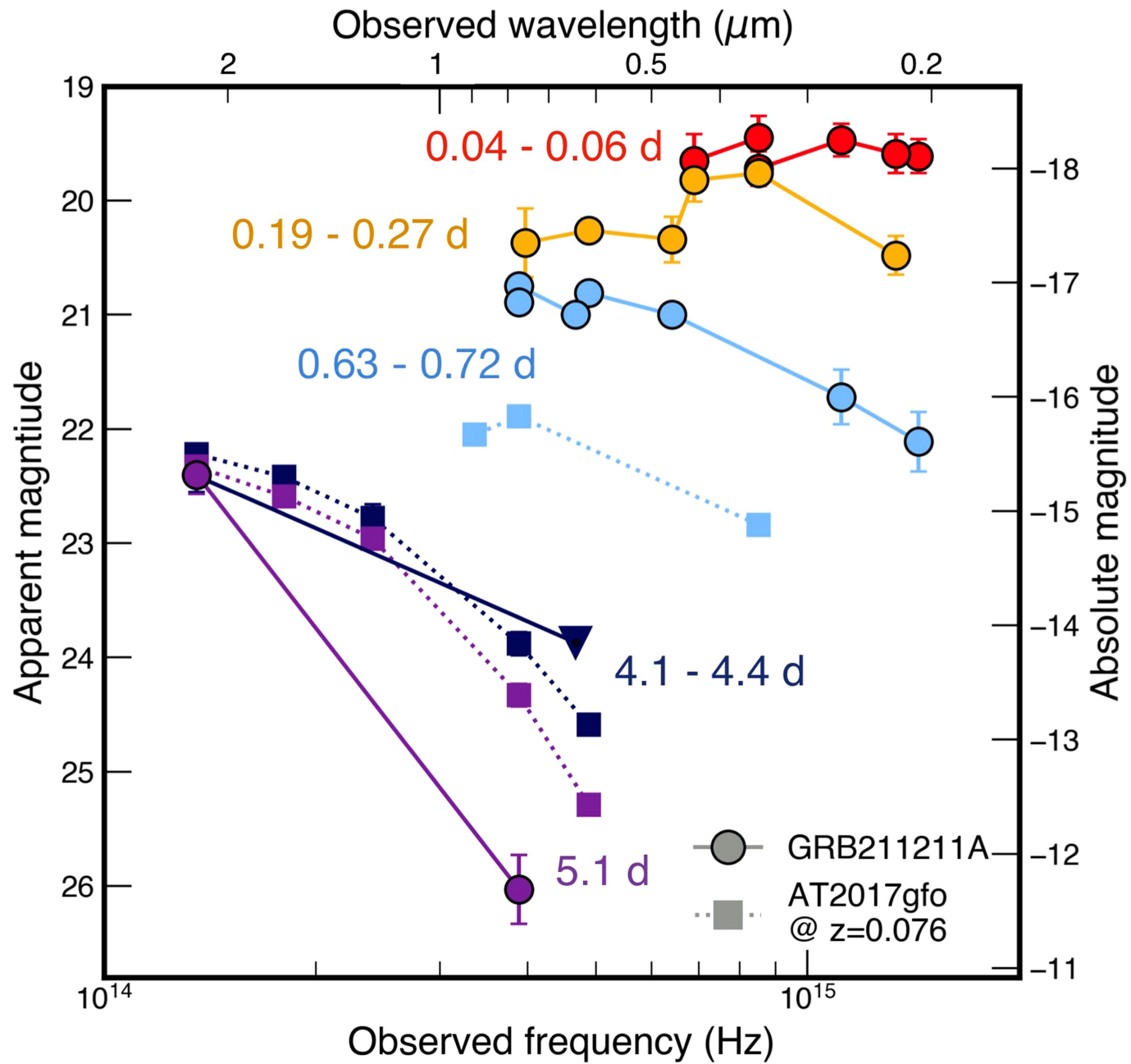
**Peer review information** *Nature* thanks the anonymous reviewers for their contribution to the peer review of this work. Peer reviewer reports are available.

**Reprints and permissions information** is available at <http://www.nature.com/reprints>.



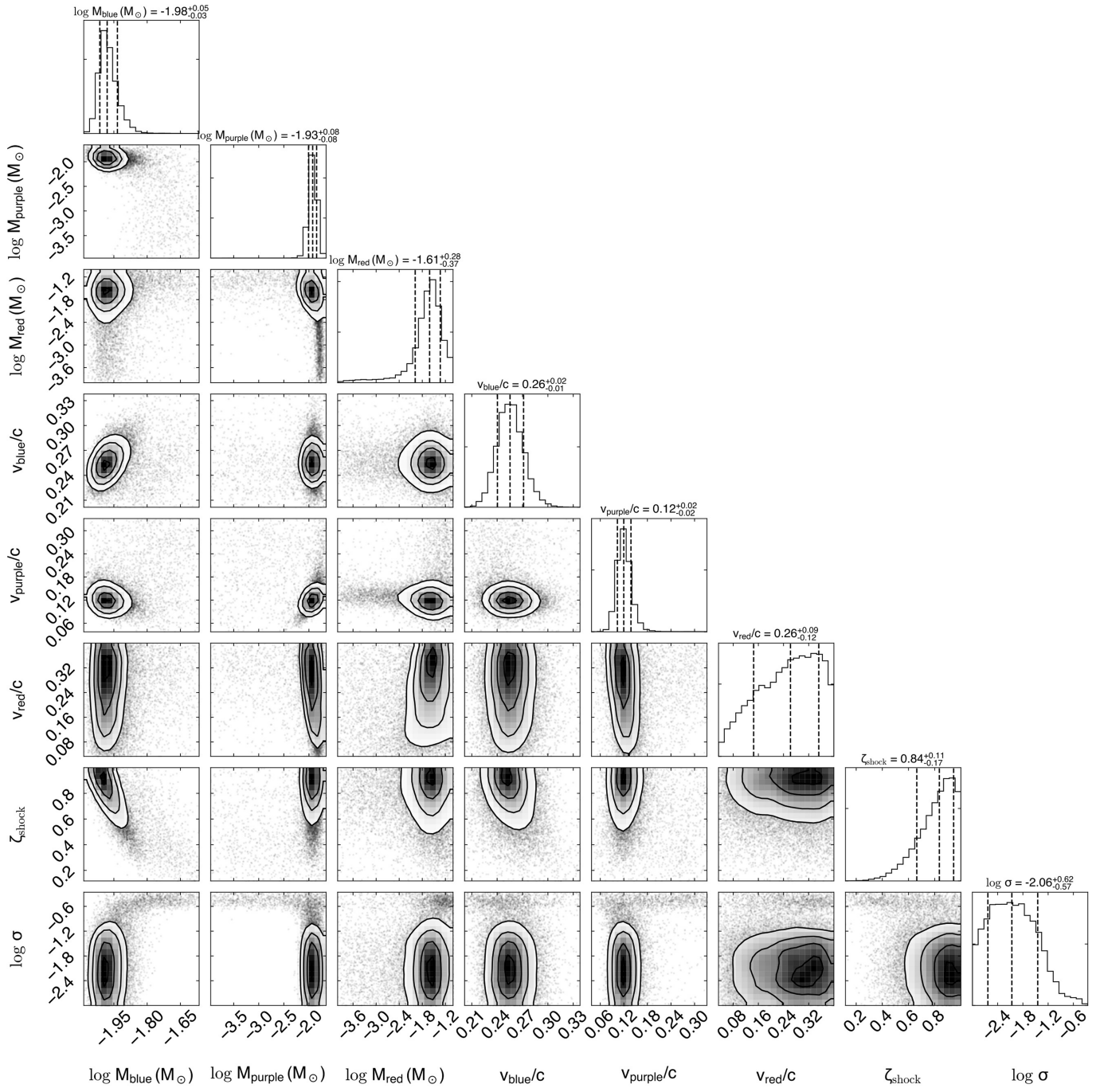
**Extended Data Fig. 1 | The host of GRB 211211A is a low-mass, actively star-forming galaxy in the local universe.** **a**, The 2D NOT/ALFOSC spectra of the afterglow and host of GRB 211211A. **b**, Keck/DEIMOS 1D spectrum (blue) and  $1\sigma$  uncertainty (dot-dashed blue line) compared with the arbitrarily scaled NOT/ALFOSC afterglow spectrum (red) and Prospectator model spectrum (grey). We highlight the strong emission lines in the observed host spectrum,

none of which are detected in the 1D or 2D afterglow spectrum. **c**, The observed host photometry (blue circles) and  $3\sigma$  uncertainties (blue lines), Prospectator model photometry (black squares) and Prospectator model spectrum (grey line). The Prospectator-derived SED matches the observed photometry, spectral continuum and spectral line strengths well.



**Extended Data Fig. 2 | Temporal evolution of the UV through NIR SED of the counterparts to GRB 211211A and GW170817.** Circles or squares represent detections, whereas triangles represent upper limits. For both GRB 211211A

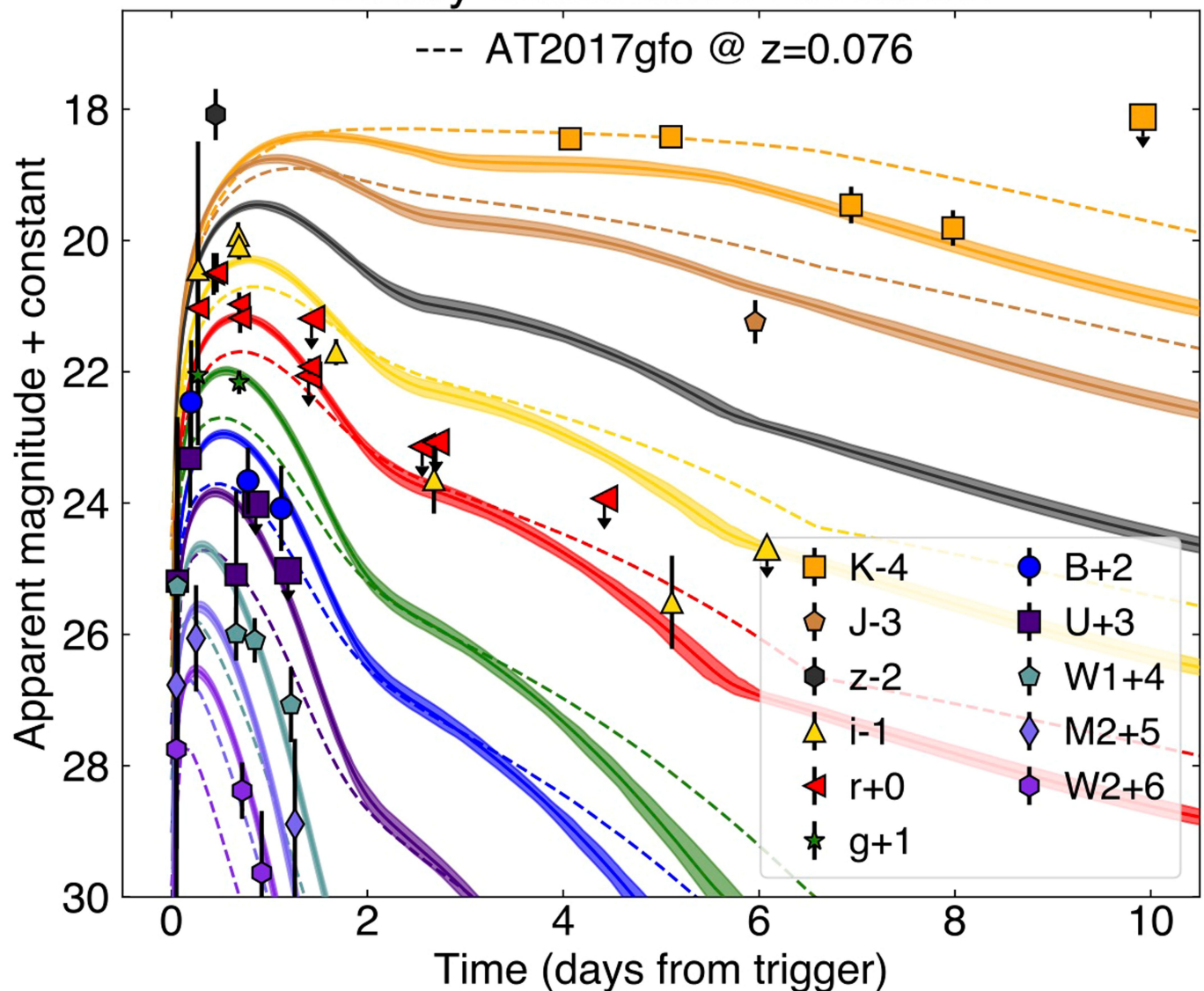
(solid lines) and GW170817 (dashed lines), the counterparts' SEDs at 4–5.1 days post-burst (dark blue and purple) demonstrate a notable reddening compared with those at earlier epochs.



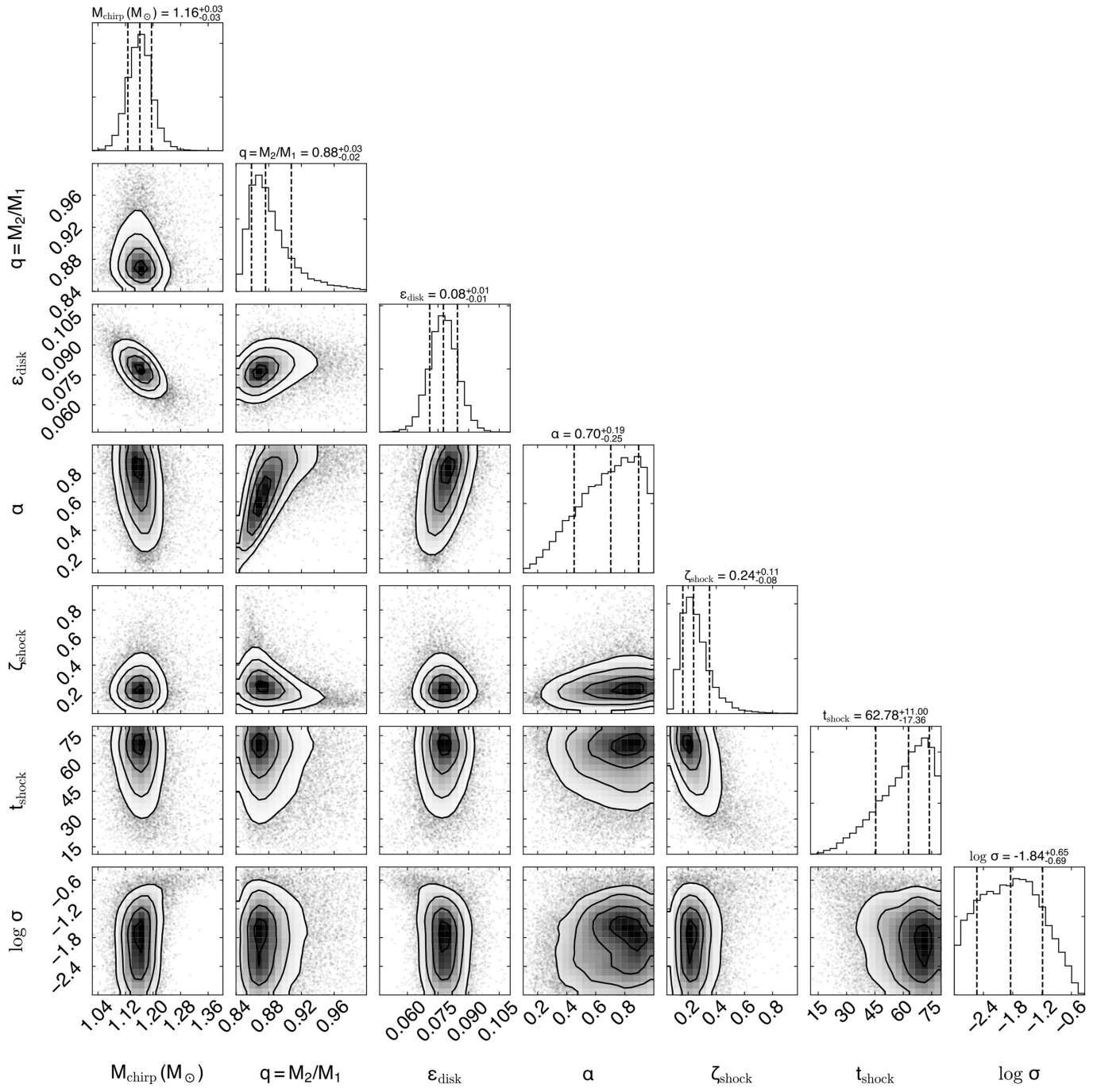
**Extended Data Fig. 3 | Corner plot showing posterior distributions for the basic kilonova model.** This model consists of three ejecta components and a fraction  $\zeta$  of the blue (low-lanthanide) ejecta that is heated by shocks from the

GRB jet. The final parameter is a white-noise term for modelling systematics in the data. The labelled  $1\sigma$  error bars are statistical only; we estimate further systematic error of about 50% on these parameters (see Methods).

# Binary-constrained KN model

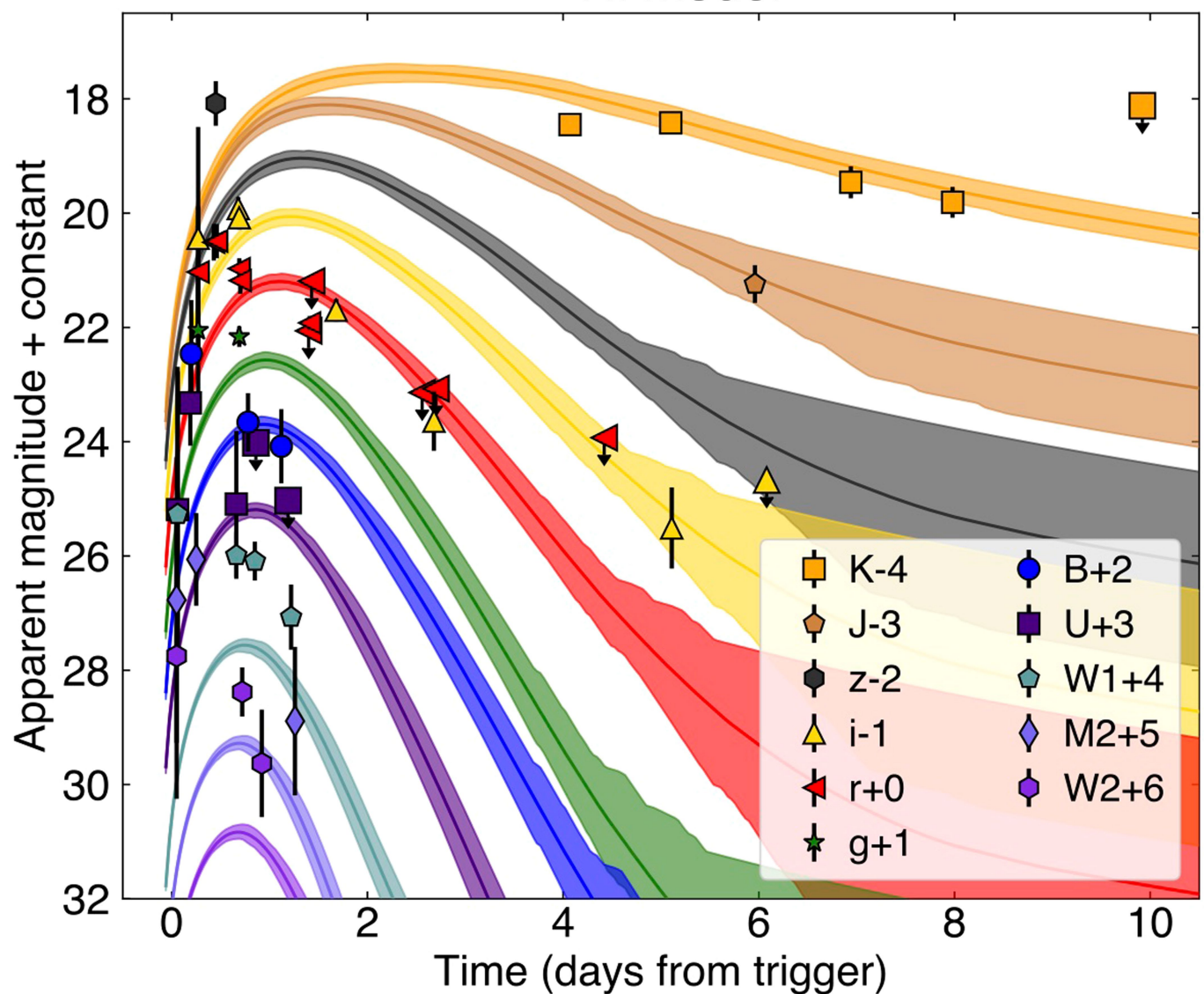


**Extended Data Fig. 4 | Light curve fit using the binary-based kilonova model<sup>21</sup>.** The dashed lines show a model for AT 2017gfo evaluated at the same redshift,  $z = 0.076$ .



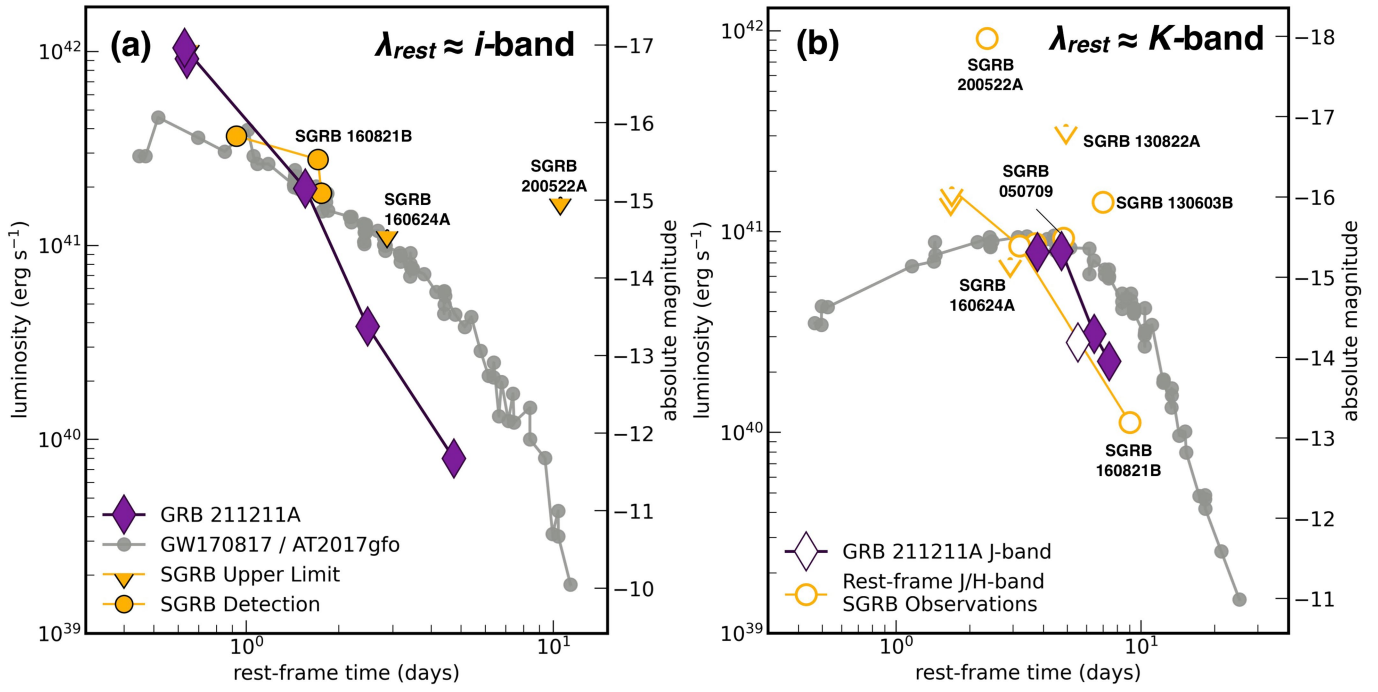
**Extended Data Fig. 5 | Corner plot showing posterior distributions for the binary-based kilonova model.** The model consists of three ejecta components whose masses, velocities and opacities depend on the chirp mass and binary mass ratio ( $q$ ) and the fraction of ejecta lost through disk ( $\varepsilon$ ) and magnetic ( $\alpha$ ) winds. A fraction  $\zeta$  of the blue (low-lanthanide) ejecta is heated by shocks from

the GRB jet over a timescale  $t_{\text{shock}}$ . The final parameter is a white-noise term for modelling systematics in the data. The labelled  $1\sigma$  error bars are statistical only; we estimate further systematic error of about 50% on these parameters (see Methods).

$^{56}\text{Ni}$  model**Extended Data Fig. 6 | Light curve fit using a  $^{56}\text{Ni}$ -powered model.**

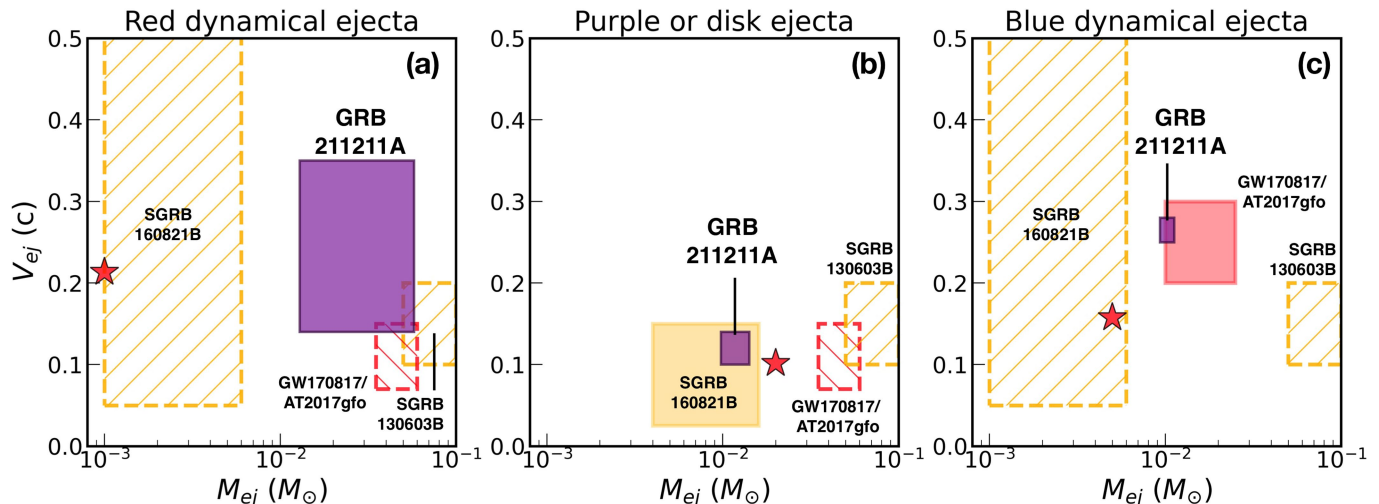
This provides a poor fit, as the single radioactive component is unable to cool quickly enough to match the early UV and longer-term NIR emission.

The best-fitting parameters require an unrealistic composition of 100%  $^{56}\text{Ni}$  and an ejecta velocity pushing against the upper bound of the prior at  $0.4c$ .



**Extended Data Fig. 7 | The optical and NIR light curves of GRB 211211A have similar luminosities and decay rates compared with past kilonovae and kilonova candidates.** The rest-frame  $i$ -band (a) and  $K$ -band (b) light curves of GRB 211211A (purple diamonds), GW170817/AT 2017gfo (grey points, ref. <sup>20</sup> and references therein) and previous short GRB kilonova upper limits

(yellow triangles) and detections (yellow circles<sup>105,147,150,151</sup>). As there are no other rest-frame  $K$ -band kilonova light curves beyond AT 2017gfo, we plot rest-frame  $J$ -band and  $H$ -band short GRB kilonova observations for comparison (open circles and triangles<sup>105,147,150–155</sup>). At  $z = 0.076$ , the  $K$ -band counterpart to GRB 211211A is of similar luminosity to AT 2017gfo and fades on similar timescales.



**Extended Data Fig. 8 | The ejecta mass and velocities estimated for GRB 211211A compared with those of past kilonovae and kilonova candidates.**

Best-fit ejecta and velocity estimates (including  $1\sigma$  errors) of the red (a), purple (b) and blue (c) kilonova components of GRB 211211A (purple boxes; Methods section ‘Kilonova model’). We also plot ejecta mass and velocity estimates for two-component models of AT 2017gfo (red boxes; compiled in ref.<sup>148</sup> and references therein), a three-component model of AT 2017gfo (red stars<sup>21</sup>) and previous short GRB kilonovae (labelled yellow boxes<sup>105,149</sup>). As two-component models of AT 2017gfo do not distinguish between the ‘purple’ and ‘red’

components included in our analysis, we plot past two-component ‘red’ estimates on both corresponding panels. We plot the dynamical ejecta estimates for GRB 160821B on the red and blue panels and the disk mass on the purple panel. We plot the total estimate for GRB 130603B on all panels. Our estimates for GRB 211211A fall within the range of AT 2017gfo and past kilonova candidates. As ejecta mass and velocity estimates are highly model-dependent, we note that the most robust comparison is between the three-component estimates for AT 2017gfo (stars) and our results for GRB 211211A.

**Extended Data Table 1 | Optical-NIR observations of the counterpart and host galaxy of GRB 211211A**

$\delta t$ (days)	Filter	Facility	Instrument	$t_{\text{exp}}$ (s)	Transient (AB mag)	AG-subtracted* (AB mag)	Host (AB mag)	Ref.
0.27	g'	MITSuME	...	6600	$20.34 \pm 0.20$	$21.05 \pm 1.07$	...	2
0.27	Rc	MITSuME	...	6600	$20.26 \pm 0.10$	$21.03 \pm 1.15$	...	2
0.27	Ic	MITSuME	...	6600	$20.37 \pm 0.30$	$21.44 \pm 1.95$	...	2
0.43	r	NEXT	...	2000	$20.25 \pm 0.07$	$20.51 \pm 0.32$	...	3
0.45	z	NEXT	...	2400	$19.88 \pm 0.30$	$20.08 \pm 0.39$	...	3
0.46	R	HCT	...	900	$20.26 \pm 0.13$	$20.49 \pm 0.30$	...	4
0.68	i	CAHA	CAFOS	2700	$20.75 \pm 0.08$	$20.92 \pm 0.20$	...	1
0.69	g	NOT	ALFOSC	240	$21.00 \pm 0.04$	$21.16 \pm 0.18$	...	1
0.69	r	NOT	ALFOSC	240	$20.81 \pm 0.05$	$20.97 \pm 0.18$	...	1
0.69	i	NOT	ALFOSC	240	$20.89 \pm 0.06$	$21.08 \pm 0.21$	...	1
0.70	R	LCO	Sinistro	1200	$21.00 \pm 0.09$	$21.18 \pm 0.23$	...	5
1.40	r	GMG	...	...	> 21.96	> 22.06	...	6
1.41	R	DOT	4Kx4K	...	$21.83 \pm 0.07$	$21.92 \pm 0.12$	...	7
1.43	r'	GIT	...	1500	> 21.15	> 21.19	...	4
1.68	i	CAHA	CAFOS	2700	$22.56 \pm 0.13$	$22.70 \pm 0.20$	...	1
2.56	Rc	Zeiss-1000	...	3600	> 23.06	> 23.14	...	8
2.68	i	CAHA	CAFOS	2400	$24.56 \pm 0.34$	$24.64 \pm 0.52$	...	1
4.07	K	Gemini	NIRI	900	$22.41 \pm 0.14$	$22.45 \pm 0.14$	...	1
4.42	R	DOT	4Kx4K	...	> 23.87	> 23.93	...	7
4.70	H	TNG	NICS	...	> 21.89	> 21.90	...	9
5.10	K	Gemini	NIRI	900	$22.40 \pm 0.17$	$22.42 \pm 0.17$	...	1
5.11	i	Gemini	GMOS	600	$26.03 \pm 0.30$	$26.51 \pm 0.71$	...	1
5.96	J	MMT	MMIRS	2400	$24.17 \pm 0.35$	$24.24 \pm 0.33$	$19.00 \pm 0.03$	1
6.08	i	Gemini	GMOS	1200	> 25.49	> 25.67	...	1
6.94	K	MMT	MMIRS	3600	$23.43 \pm 0.31$	$23.46 \pm 0.28$	...	1
7.98	K	MMT	MMIRS	2250	$23.77 \pm 0.30$	$23.81 \pm 0.27$	$19.22 \pm 0.07$	1
9.92	K	MMT	MMIRS	1170	> 22.11	> 22.12	...	1
17.65	i	NOT	ALFOSC	3000	> 24.67	...	...	1
19.57	i	CAHA	CAFOS	4000	> 24.14	...	...	1
46.94	g	MMT	Binospec	600	> 24.72	...	$19.78 \pm 0.06$	1
46.95	r	MMT	Binospec	600	> 24.48	...	$19.42 \pm 0.04$	1
46.97	z	MMT	Binospec	600	> 23.92	...	$19.18 \pm 0.08$	1
55.03	i	Gemini	GMOS	2640	> 26.77	...	$19.16 \pm 0.05$	1
65.95	$K_s$	GTC	EMIR	3528	> 21.99	...	...	1
88.82	$K_s$	LBT	LUCI	7229	> 24.62	...	...	1
97.85	K	MMT	MMIRS	3600	> 24.32	...	...	1
122.18	F140W	HST	WFC3/IR	2412	> 27.19	...	$18.95 \pm 0.01$	1
123.54	F606W	HST	ACS/WFC	2000	> 27.76	...	$19.53 \pm 0.01$	1
Arch.	u	SDSS	...	...	...	...	$20.86 \pm 0.13$	10
Arch.	W1	WISE	...	...	...	...	$19.76 \pm 0.05$	11

Asterisk \* indicates magnitudes of the transient after subtracting the model afterglow flux as described in Methods. Magnitudes corrected for foreground galactic extinction according to  $A_v=0.048$  mag (ref.<sup>84</sup>). All upper limits newly published in this work are given at the  $3\sigma$  level. References: (1) This work, (2)<sup>156</sup>, (3)<sup>157</sup>, (4)<sup>158</sup>, (5)<sup>159</sup>, (6)<sup>160</sup>, (7)<sup>161</sup>, (8)<sup>162</sup>, (9)<sup>163</sup>, (10)<sup>66</sup>, (11)<sup>81</sup>. This table is available in a machine-readable format in the Supplementary Information.

# Article

**Extended Data Table 2 | Swift/UVOT photometry of the counterpart to GRB 211211A**

$\delta t$ (days)	Band	$t_{\text{exp}}$ (s)	Transient (AB mag)	AG-subtracted* (AB mag)
0.05	<i>v</i>	199.8	$19.17 \pm 0.29$	$22.41 \pm 2.50$
0.73	<i>v</i>	189.8	$> 19.21$	$> 19.24$
0.92	<i>v</i>	186.6	$> 19.20$	$> 19.22$
0.04	<i>b</i>	199.8	$19.65 \pm 0.23$	$> 18.05$
0.20	<i>b</i>	600.6	$19.82 \pm 0.19$	$20.46 \pm 0.94$
0.78	<i>b</i>	906.9	$21.47 \pm 0.48$	$21.66 \pm 0.51$
1.12	<i>b</i>	12553.7	$> 20.63$	$22.08 \pm 0.65$
0.04	<i>u</i>	199.8	$19.72 \pm 0.15$	$> 18.13$
0.06	<i>u</i>	80.0	$19.45 \pm 0.19$	$22.19 \pm 2.50$
0.19	<i>u</i>	906.8	$19.76 \pm 0.07$	$20.32 \pm 0.75$
0.66	<i>u</i>	184.5	$> 20.36$	$22.09 \pm 1.28$
0.86	<i>u</i>	183.7	$> 20.94$	$> 21.02$
1.19	<i>u</i>	906.6	$> 21.92$	$> 22.03$
0.06	<i>uvw1</i>	199.8	$19.47 \pm 0.14$	$21.27 \pm 2.50$
0.66	<i>uvw1</i>	899.8	$21.72 \pm 0.24$	$21.99 \pm 0.41$
0.85	<i>uvw1</i>	899.8	$21.91 \pm 0.27$	$22.09 \pm 0.34$
1.22	<i>uvw1</i>	17535.0	$> 21.98$	$23.07 \pm 0.57$
0.05	<i>uvm2</i>	199.7	$19.59 \pm 0.17$	$21.77 \pm 2.50$
0.25	<i>uvm2</i>	474.7	$20.48 \pm 0.17$	$21.06 \pm 0.81$
1.26	<i>uvm2</i>	826.4	$> 22.18$	$23.89 \pm 1.30$
0.05	<i>uvw2</i>	199.8	$19.61 \pm 0.15$	$21.75 \pm 2.50$
0.72	<i>uvw2</i>	899.8	$22.11 \pm 0.26$	$22.38 \pm 0.43$
0.92	<i>uvw2</i>	899.8	$> 22.23$	$23.63 \pm 0.94$
0.00	<i>white</i>	149.8	$20.69 \pm 0.24$	$24.11 \pm 2.50$
0.79	<i>white</i>	182.5	$21.74 \pm 0.35$	$21.95 \pm 0.44$
1.06	<i>white</i>	181.5	$21.59 \pm 0.36$	$21.69 \pm 0.36$
1.78	<i>white</i>	25045.5	$23.41 \pm 0.30$	$23.59 \pm 0.37$
Host				
	<i>v</i>		$> 19.78$	
	<i>b</i>		$20.51 \pm 0.14$	
	<i>u</i>		$21.21 \pm 0.19$	
	<i>uvw1</i>		$21.66 \pm 0.13$	
	<i>uvm2</i>		$21.86 \pm 0.13$	
	<i>uvw2</i>		$21.87 \pm 0.17$	

\*Magnitudes of the transient after subtracting the model afterglow flux as described in Methods. Magnitudes corrected for foreground galactic extinction according to  $A_v=0.048\text{mag}$  (ref. <sup>84</sup>). This table is available in a machine-readable format in the Supplementary Information.

Extended Data Table 3 | Afterglow modelling parameters

Parameter	Median	Units
$\log(E_{\text{K,iso}})$	$52.71^{+0.75}_{-0.78}$	erg
$\Gamma_0$	$73.11^{+51.70}_{-22.08}$	
$p$	$2.014^{+0.007}_{-0.003}$	
$\iota$	$0.688^{+0.401}_{-0.344}$	deg
$\log(n)$	$-0.265^{+1.289}_{-1.925}$	cm <sup>-3</sup>
$\theta_c$	$2.750^{+1.261}_{-1.432}$	deg
$\log(\varepsilon_e)$	$-1.484^{+0.742}_{-0.807}$	
$\log(\epsilon_B)$	$-3.819^{+1.535}_{-1.312}$	

Corresponding author(s): Jillian Rastinejad

Last updated by author(s): Aug 26, 2022

## Reporting Summary

Nature Portfolio wishes to improve the reproducibility of the work that we publish. This form provides structure for consistency and transparency in reporting. For further information on Nature Portfolio policies, see our [Editorial Policies](#) and the [Editorial Policy Checklist](#).

### Statistics

For all statistical analyses, confirm that the following items are present in the figure legend, table legend, main text, or Methods section.

n/a Confirmed

- The exact sample size ( $n$ ) for each experimental group/condition, given as a discrete number and unit of measurement
- A statement on whether measurements were taken from distinct samples or whether the same sample was measured repeatedly
- The statistical test(s) used AND whether they are one- or two-sided  
*Only common tests should be described solely by name; describe more complex techniques in the Methods section.*
- A description of all covariates tested
- A description of any assumptions or corrections, such as tests of normality and adjustment for multiple comparisons
- A full description of the statistical parameters including central tendency (e.g. means) or other basic estimates (e.g. regression coefficient) AND variation (e.g. standard deviation) or associated estimates of uncertainty (e.g. confidence intervals)
- For null hypothesis testing, the test statistic (e.g.  $F$ ,  $t$ ,  $r$ ) with confidence intervals, effect sizes, degrees of freedom and  $P$  value noted  
*Give P values as exact values whenever suitable.*
- For Bayesian analysis, information on the choice of priors and Markov chain Monte Carlo settings
- For hierarchical and complex designs, identification of the appropriate level for tests and full reporting of outcomes
- Estimates of effect sizes (e.g. Cohen's  $d$ , Pearson's  $r$ ), indicating how they were calculated

*Our web collection on [statistics for biologists](#) contains articles on many of the points above.*

### Software and code

Policy information about [availability of computer code](#)

Data collection

Optical and Near-IR observations were obtained with the Gemini Observatory, the MMT Observatory, the W. M. Keck Observatory, the Hubble Space Telescope, Gran Telescopio Canarias, the Nordic Optical Telescope, the Large Binocular Telescope and Calar Alto Astronomical Observatory. Radio observations were obtained with the Very Large Array. Specific data reduction methods are described and cited in the Methods section. Additional observations are gathered from the Gamma-ray Circular Notices (GCNs) and cited in Extended Data Table 1. Gamma-ray and X-ray light curves may be downloaded from the UK Swift Science Data Centre and the online HEARSAC archive at <https://heasarc.gsfc.nasa.gov/W3Browse/fermi/fermigrbst.html>.

Data analysis

The kilonova model scripts are available at <https://github.com/guilochon/MOSFiT>. The scripts used to model the afterglow will be publicly available upon publication of this manuscript. The Prospector stellar population modeling code is available at <https://github.com/bd-j/prospector>.

For manuscripts utilizing custom algorithms or software that are central to the research but not yet described in published literature, software must be made available to editors and reviewers. We strongly encourage code deposition in a community repository (e.g. GitHub). See the Nature Portfolio [guidelines for submitting code & software](#) for further information.

## Data

Policy information about [availability of data](#)

All manuscripts must include a [data availability statement](#). This statement should provide the following information, where applicable:

- Accession codes, unique identifiers, or web links for publicly available datasets
- A description of any restrictions on data availability
- For clinical datasets or third party data, please ensure that the statement adheres to our [policy](#)

The majority of data generated or analysed during this study are included in this article's Extended Data Tables. Gamma-ray and X-ray light curves may be downloaded from the UK Swift}Science Data Centre and the online HEARSAC archive at <https://heasarc.gsfc.nasa.gov/W3Browse/fermi/fermigrbst.html>.

## Human research participants

Policy information about [studies involving human research participants](#) and [Sex and Gender in Research](#).

### Reporting on sex and gender

*Use the terms sex (biological attribute) and gender (shaped by social and cultural circumstances) carefully in order to avoid confusing both terms. Indicate if findings apply to only one sex or gender; describe whether sex and gender were considered in study design whether sex and/or gender was determined based on self-reporting or assigned and methods used. Provide in the source data disaggregated sex and gender data where this information has been collected, and consent has been obtained for sharing of individual-level data; provide overall numbers in this Reporting Summary. Please state if this information has not been collected. Report sex- and gender-based analyses where performed, justify reasons for lack of sex- and gender-based analysis.*

### Population characteristics

*Describe the covariate-relevant population characteristics of the human research participants (e.g. age, genotypic information, past and current diagnosis and treatment categories). If you filled out the behavioural & social sciences study design questions and have nothing to add here, write "See above."*

### Recruitment

*Describe how participants were recruited. Outline any potential self-selection bias or other biases that may be present and how these are likely to impact results.*

### Ethics oversight

*Identify the organization(s) that approved the study protocol.*

Note that full information on the approval of the study protocol must also be provided in the manuscript.

## Field-specific reporting

Please select the one below that is the best fit for your research. If you are not sure, read the appropriate sections before making your selection.

Life sciences       Behavioural & social sciences       Ecological, evolutionary & environmental sciences

For a reference copy of the document with all sections, see [nature.com/documents/nr-reporting-summary-flat.pdf](https://nature.com/documents/nr-reporting-summary-flat.pdf)

## Life sciences study design

All studies must disclose on these points even when the disclosure is negative.

### Sample size

*Describe how sample size was determined, detailing any statistical methods used to predetermine sample size OR if no sample-size calculation was performed, describe how sample sizes were chosen and provide a rationale for why these sample sizes are sufficient.*

### Data exclusions

*Describe any data exclusions. If no data were excluded from the analyses, state so OR if data were excluded, describe the exclusions and the rationale behind them, indicating whether exclusion criteria were pre-established.*

### Replication

*Describe the measures taken to verify the reproducibility of the experimental findings. If all attempts at replication were successful, confirm this OR if there are any findings that were not replicated or cannot be reproduced, note this and describe why.*

### Randomization

*Describe how samples/organisms/participants were allocated into experimental groups. If allocation was not random, describe how covariates were controlled OR if this is not relevant to your study, explain why.*

### Blinding

*Describe whether the investigators were blinded to group allocation during data collection and/or analysis. If blinding was not possible, describe why OR explain why blinding was not relevant to your study.*

# Behavioural & social sciences study design

All studies must disclose on these points even when the disclosure is negative.

Study description	Briefly describe the study type including whether data are quantitative, qualitative, or mixed-methods (e.g. qualitative cross-sectional, quantitative experimental, mixed-methods case study).
Research sample	State the research sample (e.g. Harvard university undergraduates, villagers in rural India) and provide relevant demographic information (e.g. age, sex) and indicate whether the sample is representative. Provide a rationale for the study sample chosen. For studies involving existing datasets, please describe the dataset and source.
Sampling strategy	Describe the sampling procedure (e.g. random, snowball, stratified, convenience). Describe the statistical methods that were used to predetermine sample size OR if no sample-size calculation was performed, describe how sample sizes were chosen and provide a rationale for why these sample sizes are sufficient. For qualitative data, please indicate whether data saturation was considered, and what criteria were used to decide that no further sampling was needed.
Data collection	Provide details about the data collection procedure, including the instruments or devices used to record the data (e.g. pen and paper, computer, eye tracker, video or audio equipment) whether anyone was present besides the participant(s) and the researcher, and whether the researcher was blind to experimental condition and/or the study hypothesis during data collection.
Timing	Indicate the start and stop dates of data collection. If there is a gap between collection periods, state the dates for each sample cohort.
Data exclusions	If no data were excluded from the analyses, state so OR if data were excluded, provide the exact number of exclusions and the rationale behind them, indicating whether exclusion criteria were pre-established.
Non-participation	State how many participants dropped out/declined participation and the reason(s) given OR provide response rate OR state that no participants dropped out/declined participation.
Randomization	If participants were not allocated into experimental groups, state so OR describe how participants were allocated to groups, and if allocation was not random, describe how covariates were controlled.

# Ecological, evolutionary & environmental sciences study design

All studies must disclose on these points even when the disclosure is negative.

Study description	Briefly describe the study. For quantitative data include treatment factors and interactions, design structure (e.g. factorial, nested, hierarchical), nature and number of experimental units and replicates.
Research sample	Describe the research sample (e.g. a group of tagged <i>Passer domesticus</i> , all <i>Stenocereus thurberi</i> within Organ Pipe Cactus National Monument), and provide a rationale for the sample choice. When relevant, describe the organism taxa, source, sex, age range and any manipulations. State what population the sample is meant to represent when applicable. For studies involving existing datasets, describe the data and its source.
Sampling strategy	Note the sampling procedure. Describe the statistical methods that were used to predetermine sample size OR if no sample-size calculation was performed, describe how sample sizes were chosen and provide a rationale for why these sample sizes are sufficient.
Data collection	Describe the data collection procedure, including who recorded the data and how.
Timing and spatial scale	Indicate the start and stop dates of data collection, noting the frequency and periodicity of sampling and providing a rationale for these choices. If there is a gap between collection periods, state the dates for each sample cohort. Specify the spatial scale from which the data are taken.
Data exclusions	If no data were excluded from the analyses, state so OR if data were excluded, describe the exclusions and the rationale behind them, indicating whether exclusion criteria were pre-established.
Reproducibility	Describe the measures taken to verify the reproducibility of experimental findings. For each experiment, note whether any attempts to repeat the experiment failed OR state that all attempts to repeat the experiment were successful.
Randomization	Describe how samples/organisms/participants were allocated into groups. If allocation was not random, describe how covariates were controlled. If this is not relevant to your study, explain why.
Blinding	Describe the extent of blinding used during data acquisition and analysis. If blinding was not possible, describe why OR explain why blinding was not relevant to your study.

Did the study involve field work?  Yes  No

## Field work, collection and transport

Field conditions	Describe the study conditions for field work, providing relevant parameters (e.g. temperature, rainfall).
Location	State the location of the sampling or experiment, providing relevant parameters (e.g. latitude and longitude, elevation, water depth).
Access & import/export	Describe the efforts you have made to access habitats and to collect and import/export your samples in a responsible manner and in compliance with local, national and international laws, noting any permits that were obtained (give the name of the issuing authority, the date of issue, and any identifying information).
Disturbance	Describe any disturbance caused by the study and how it was minimized.

## Reporting for specific materials, systems and methods

We require information from authors about some types of materials, experimental systems and methods used in many studies. Here, indicate whether each material, system or method listed is relevant to your study. If you are not sure if a list item applies to your research, read the appropriate section before selecting a response.

Materials & experimental systems		Methods	
n/a	Involved in the study	n/a	Involved in the study
<input type="checkbox"/>	Antibodies	<input type="checkbox"/>	ChIP-seq
<input type="checkbox"/>	Eukaryotic cell lines	<input type="checkbox"/>	Flow cytometry
<input type="checkbox"/>	Palaeontology and archaeology	<input type="checkbox"/>	MRI-based neuroimaging
<input type="checkbox"/>	Animals and other organisms		
<input type="checkbox"/>	Clinical data		
<input type="checkbox"/>	Dual use research of concern		

## Antibodies

Antibodies used	Describe all antibodies used in the study; as applicable, provide supplier name, catalog number, clone name, and lot number.
Validation	Describe the validation of each primary antibody for the species and application, noting any validation statements on the manufacturer's website, relevant citations, antibody profiles in online databases, or data provided in the manuscript.

## Eukaryotic cell lines

Policy information about [cell lines and Sex and Gender in Research](#)

Cell line source(s)	State the source of each cell line used and the sex of all primary cell lines and cells derived from human participants or vertebrate models.
Authentication	Describe the authentication procedures for each cell line used OR declare that none of the cell lines used were authenticated.
Mycoplasma contamination	Confirm that all cell lines tested negative for mycoplasma contamination OR describe the results of the testing for mycoplasma contamination OR declare that the cell lines were not tested for mycoplasma contamination.
Commonly misidentified lines (See <a href="#">ICLAC</a> register)	Name any commonly misidentified cell lines used in the study and provide a rationale for their use.

## Palaeontology and Archaeology

Specimen provenance	Provide provenance information for specimens and describe permits that were obtained for the work (including the name of the issuing authority, the date of issue, and any identifying information). Permits should encompass collection and, where applicable, export.
Specimen deposition	Indicate where the specimens have been deposited to permit free access by other researchers.

**Dating methods**

If new dates are provided, describe how they were obtained (e.g. collection, storage, sample pretreatment and measurement), where they were obtained (i.e. lab name), the calibration program and the protocol for quality assurance OR state that no new dates are provided.

Tick this box to confirm that the raw and calibrated dates are available in the paper or in Supplementary Information.

**Ethics oversight**

Identify the organization(s) that approved or provided guidance on the study protocol, OR state that no ethical approval or guidance was required and explain why not.

Note that full information on the approval of the study protocol must also be provided in the manuscript.

## Animals and other research organisms

Policy information about [studies involving animals; ARRIVE guidelines](#) recommended for reporting animal research, and [Sex and Gender in Research](#)

**Laboratory animals**

For laboratory animals, report species, strain and age OR state that the study did not involve laboratory animals.

**Wild animals**

Provide details on animals observed in or captured in the field; report species and age where possible. Describe how animals were caught and transported and what happened to captive animals after the study (if killed, explain why and describe method; if released, say where and when) OR state that the study did not involve wild animals.

**Reporting on sex**

Indicate if findings apply to only one sex; describe whether sex was considered in study design, methods used for assigning sex. Provide data disaggregated for sex where this information has been collected in the source data as appropriate; provide overall numbers in this Reporting Summary. Please state if this information has not been collected. Report sex-based analyses where performed, justify reasons for lack of sex-based analysis.

**Field-collected samples**

For laboratory work with field-collected samples, describe all relevant parameters such as housing, maintenance, temperature, photoperiod and end-of-experiment protocol OR state that the study did not involve samples collected from the field.

**Ethics oversight**

Identify the organization(s) that approved or provided guidance on the study protocol, OR state that no ethical approval or guidance was required and explain why not.

Note that full information on the approval of the study protocol must also be provided in the manuscript.

## Clinical data

Policy information about [clinical studies](#)

All manuscripts should comply with the [ICMJE guidelines for publication of clinical research](#) and a completed [CONSORT checklist](#) must be included with all submissions.

**Clinical trial registration**

Provide the trial registration number from ClinicalTrials.gov or an equivalent agency.

**Study protocol**

Note where the full trial protocol can be accessed OR if not available, explain why.

**Data collection**

Describe the settings and locales of data collection, noting the time periods of recruitment and data collection.

**Outcomes**

Describe how you pre-defined primary and secondary outcome measures and how you assessed these measures.

## Dual use research of concern

Policy information about [dual use research of concern](#)

### Hazards

Could the accidental, deliberate or reckless misuse of agents or technologies generated in the work, or the application of information presented in the manuscript, pose a threat to:

No	Yes
<input type="checkbox"/>	Public health
<input type="checkbox"/>	National security
<input type="checkbox"/>	Crops and/or livestock
<input type="checkbox"/>	Ecosystems
<input type="checkbox"/>	Any other significant area

## Experiments of concern

Does the work involve any of these experiments of concern:

- | No                       | Yes  |
|--------------------------|--|
| <input type="checkbox"/> | <input type="checkbox"/> Demonstrate how to render a vaccine ineffective                             |
| <input type="checkbox"/> | <input type="checkbox"/> Confer resistance to therapeutically useful antibiotics or antiviral agents |
| <input type="checkbox"/> | <input type="checkbox"/> Enhance the virulence of a pathogen or render a nonpathogen virulent        |
| <input type="checkbox"/> | <input type="checkbox"/> Increase transmissibility of a pathogen                                     |
| <input type="checkbox"/> | <input type="checkbox"/> Alter the host range of a pathogen  |
| <input type="checkbox"/> | <input type="checkbox"/> Enable evasion of diagnostic/detection modalities                           |
| <input type="checkbox"/> | <input type="checkbox"/> Enable the weaponization of a biological agent or toxin                     |
| <input type="checkbox"/> | <input type="checkbox"/> Any other potentially harmful combination of experiments and agents         |

## ChIP-seq

### Data deposition

- Confirm that both raw and final processed data have been deposited in a public database such as [GEO](#).
- Confirm that you have deposited or provided access to graph files (e.g. BED files) for the called peaks.

#### Data access links

*May remain private before publication.*

For "Initial submission" or "Revised version" documents, provide reviewer access links. For your "Final submission" document, provide a link to the deposited data.

#### Files in database submission

Provide a list of all files available in the database submission.

#### Genome browser session (e.g. [UCSC](#))

Provide a link to an anonymized genome browser session for "Initial submission" and "Revised version" documents only, to enable peer review. Write "no longer applicable" for "Final submission" documents.

## Methodology

### Replicates

Describe the experimental replicates, specifying number, type and replicate agreement.

### Sequencing depth

Describe the sequencing depth for each experiment, providing the total number of reads, uniquely mapped reads, length of reads and whether they were paired- or single-end.

### Antibodies

Describe the antibodies used for the ChIP-seq experiments; as applicable, provide supplier name, catalog number, clone name, and lot number.

### Peak calling parameters

Specify the command line program and parameters used for read mapping and peak calling, including the ChIP, control and index files used.

### Data quality

Describe the methods used to ensure data quality in full detail, including how many peaks are at FDR 5% and above 5-fold enrichment.

### Software

Describe the software used to collect and analyze the ChIP-seq data. For custom code that has been deposited into a community repository, provide accession details.

## Flow Cytometry

### Plots

Confirm that:

- The axis labels state the marker and fluorochrome used (e.g. CD4-FITC).
- The axis scales are clearly visible. Include numbers along axes only for bottom left plot of group (a 'group' is an analysis of identical markers).
- All plots are contour plots with outliers or pseudocolor plots.
- A numerical value for number of cells or percentage (with statistics) is provided.

## Methodology

### Sample preparation

Describe the sample preparation, detailing the biological source of the cells and any tissue processing steps used.

### Instrument

Identify the instrument used for data collection, specifying make and model number.

**Software**

*Describe the software used to collect and analyze the flow cytometry data. For custom code that has been deposited into a community repository, provide accession details.*

**Cell population abundance**

*Describe the abundance of the relevant cell populations within post-sort fractions, providing details on the purity of the samples and how it was determined.*

**Gating strategy**

*Describe the gating strategy used for all relevant experiments, specifying the preliminary FSC/SSC gates of the starting cell population, indicating where boundaries between "positive" and "negative" staining cell populations are defined.*

Tick this box to confirm that a figure exemplifying the gating strategy is provided in the Supplementary Information.

## Magnetic resonance imaging

### Experimental design

**Design type**

*Indicate task or resting state; event-related or block design.*

**Design specifications**

*Specify the number of blocks, trials or experimental units per session and/or subject, and specify the length of each trial or block (if trials are blocked) and interval between trials.*

**Behavioral performance measures**

*State number and/or type of variables recorded (e.g. correct button press, response time) and what statistics were used to establish that the subjects were performing the task as expected (e.g. mean, range, and/or standard deviation across subjects).*

### Acquisition

**Imaging type(s)**

*Specify: functional, structural, diffusion, perfusion.*

**Field strength**

*Specify in Tesla*

**Sequence & imaging parameters**

*Specify the pulse sequence type (gradient echo, spin echo, etc.), imaging type (EPI, spiral, etc.), field of view, matrix size, slice thickness, orientation and TE/TR/flip angle.*

**Area of acquisition**

*State whether a whole brain scan was used OR define the area of acquisition, describing how the region was determined.*

**Diffusion MRI**

Used

Not used

### Preprocessing

**Preprocessing software**

*Provide detail on software version and revision number and on specific parameters (model/functions, brain extraction, segmentation, smoothing kernel size, etc.).*

**Normalization**

*If data were normalized/standardized, describe the approach(es): specify linear or non-linear and define image types used for transformation OR indicate that data were not normalized and explain rationale for lack of normalization.*

**Normalization template**

*Describe the template used for normalization/transformation, specifying subject space or group standardized space (e.g. original Talairach, MNI305, ICBM152) OR indicate that the data were not normalized.*

**Noise and artifact removal**

*Describe your procedure(s) for artifact and structured noise removal, specifying motion parameters, tissue signals and physiological signals (heart rate, respiration).*

**Volume censoring**

*Define your software and/or method and criteria for volume censoring, and state the extent of such censoring.*

### Statistical modeling & inference

**Model type and settings**

*Specify type (mass univariate, multivariate, RSA, predictive, etc.) and describe essential details of the model at the first and second levels (e.g. fixed, random or mixed effects; drift or auto-correlation).*

**Effect(s) tested**

*Define precise effect in terms of the task or stimulus conditions instead of psychological concepts and indicate whether ANOVA or factorial designs were used.*

**Specify type of analysis:**

Whole brain     ROI-based     Both

**Statistic type for inference  
(See [Eklund et al. 2016](#))**

*Specify voxel-wise or cluster-wise and report all relevant parameters for cluster-wise methods.*

**Correction**

*Describe the type of correction and how it is obtained for multiple comparisons (e.g. FWE, FDR, permutation or Monte Carlo).*

## Models & analysis

n/a Involved in the study

Functional and/or effective connectivity

Graph analysis

Multivariate modeling or predictive analysis

Functional and/or effective connectivity

*Report the measures of dependence used and the model details (e.g. Pearson correlation, partial correlation, mutual information).*

Graph analysis

*Report the dependent variable and connectivity measure, specifying weighted graph or binarized graph, subject- or group-level, and the global and/or node summaries used (e.g. clustering coefficient, efficiency, etc.).*

Multivariate modeling and predictive analysis

*Specify independent variables, features extraction and dimension reduction, model, training and evaluation metrics.*